MERIS ATBD 2.24

Vicarious adjustment of the MERIS Ocean Colour Radiometry

Ref.: MERIS ATBD 2.24

Issue: 1. 0

Date: 29/09/2011

Preparation and signature list

	Name and role	Company	Signature
Prepared by	C. Lerebourg	ACRI-ST	
	C. Mazeran	ACRI-ST	
	J.P. Huot	ESA	
	D. Antoine	LOV	

Distribution List

Company	To
	Public distribution

Change log

Version	Date	Changes
1.0	29/09/2011	Initial version

Table of Content

List of Figures

List of Tables

Acknowledgements

We thank Francis Zagolski (Parbleu Technologies) for his helpful radiative transfer simulations database MEROS used in our validation (Santer and Zagolski 2010). We also thank the team at ESA, ACRI and ARGANS for the MERMAID facility (http://hermes.acri.fr/mermaid) and we particularly gratefully acknowledge the following Principle Investigators who provide extremely valuable *in situ* data:

Giuseppe Zibordi (Joint Research Center, Italy) for the following AERONET- OC sites: Acqua Alta Oceanographic Tower, Abu Al Bukhoosh, Gustav Dalen Tower and Helsinki Lighthouse (Zibordi *et al.* 2009a, Zibordi *et al.* 2009b);

John Icely (University of Algarve, Portugal) for the Sagres coast dataset (Cristina *et al.* 2009);

David Antoine (Laboratoire d'Océanographie de Villefranche, France) for the BOUSSOLE dataset, used in particular for the vicarious adjustment (Antoine *et al.* 2006, Antoine *et al.* 2008);

David McKee (University of Strathclyde, UK) for the Bristol Channel and Irish Sea datasets;

Mati Kahru (University of California, US) for the California Current dataset;

Hubert Loisel (Laboratoire d'Océanologie et de Géosciences, France) for the East English Channel and French Guiana datasets (Loisel *et al.* 2007, Lubac *et al.* 2007) ;

Michael Ondrusek (NOAA) for the MOBY dataset used for the vicarious adjustment (Clark *et al.* 2003);

Kevin Ruddick (MUMM, Belgium) for the MUMMTriOS dataset (Ruddick *et al.* 2006);

Doug Vandemark and Hui Feng (University of New Hampshire, US) for the AERONET-OC MVCO dataset (Zibordi *et al.* 2009);

Jeremy Werdell (NASA), Larry Harding (University of Maryland, US), Antonio Mannino (NASA), Ajit Subramaniam (University of Maryland, US), Dariusz Stramski (University of California, US), Greg Mitchell (University of California, US), William Balch (Bigelow Laboratory for Ocean Sciences, US), Frank Muller-Karger (University South Florida, US), Ru Morrison (Woods Hole Oceanographic Institution, US), Zhongping Lee (Naval Research Laboratory), Ken Carder (Professor Emeritus University South Florida, US), Norman Nelson (University of California, US), Richard Gould (Naval Research Laboratory, US), Robert Arnone (Naval Research Laboratory, US) and Stan Hooker (NASA) for the NOMAD dataset (Werdell *et al.* 2005);

Suzanne Kratzer (University of Stockholm, Sweden) for the North-Western Baltic Sea and AERONET-OC Palgrunden dataset (Kratzer *et al.* 2008);

David Siegel (University of California, US) for the Plumes and Blooms dataset;

Pierre-Yves Deschamps (Laboratoire d'Optique Appliquée, France) for the SIMBADA dataset ;

Annelies Hommersom (IVM, Netherlands) for the Wadden Sea dataset.

1 Introduction

1.1 Scope of the document

This Algorithm Theoretical Basis Document 2.24 describes the vicarious adjustment of the MERIS ocean colour radiometry, implemented for the first time in the Level 2 chain at the occasion of the 3rd data reprocessing.

It presents the method, its validation against *in situ* data and provides the fifteen adjustment factors used in the 3rd reprocessing configuration and available in the nominal configuration of the ODESA processor.

1.2 Acronyms

The following table provides the definition of the acronyms used in this document.

Acronym	Definition
ATBD	Algorithm Theoretical Basis Document
BPAC	Bright Pixel Atmospheric Correction
CCD	Charged-Coupled Device
ESA	European Space Agency
LUT	Look-Up Table
MEGS	MERIS Ground Segment prototype
MERIS	MEdium Range Imaging Spectrometer
MERMAID	MERIS Matchup In Situ Database
NIR	Near Infra-Red
OCL	Offset Control Loop
OCR	Ocean Colour Radiometry
ODESA	Optical Data processor of ESA
RR	Reduced Resolution
SeaWiFS	Sea-viewing Wide Field-of-view Sensor
SSA	Single Scattering Approximation
SIO	South Indian Ocean
SOS	Successive Order of Scattering
SPG	South Pacific Gyre
TOA	Top Of Atmosphere
VIS	Visible part of the spectrum

1.3 Notations

The following table provides the definition of the notations used in this document.

Symbol	Definition	Units
i	Index for a target measurement (location and time)	Dimensionless
$g(\lambda)$	Individual adjustment factor for target *i*	Dimensionless
$\bar{g}(\lambda)$	Averaged adjustment factor over all targets	Dimensionless
$L_{TOA}(\lambda)$	Level 1 TOA radiance	mW m^{-2} nm^{-1} sr^{-1}
$L_w(\lambda)$	Water radiance	mW m^{-2} nm^{-1} sr^{-1}
N	Number of matchups used to compute the gain	Dimensionless
$t_d(\lambda)$	Total (direct and diffuse) transmittance	Dimensionless
$t_d^{vic}(\lambda)$	Total transmittance after NIR adjustment	Dimensionless
ε	Spectral depence of the aerosol reflectance in the single scattering approximation	Dimensionless
λ	Wavelength	nm
λ_{ref}	Reference wavelength for the NIR adjustment	nm
$\rho_{aer}(\lambda)$	Aerosol reflectance	Dimensionless
$\rho_{gc}(\lambda)$	TOA reflectance corrected for gaseous absorption, smile effect and glint	Dimensionless
$\rho_{gc}^{t}(\lambda)$	Targeted ρ_{gc} reflectance	Dimensionless
$\rho_{gc}^{vic}(\lambda)$	Vicarious adjusted ρ_{gc} reflectance	Dimensionless
$\rho_{ng}^{*}(\lambda)$	TOA reflectance corrected for gaseous absorption and smile effect	Dimensionless
$\rho_{path}(\lambda)$	Atmospheric path reflectance	Dimensionless
$\rho_{path}^{vic}(\lambda)$	Atmospheric path reflectance after NIR adjustment	Dimensionless
$\rho_R(\lambda)$	Rayleigh reflectance	Dimensionless
$\rho_{TOA}(\lambda)$	TOA reflectance	Dimensionless
$\rho_w(\lambda)$	Water reflectance	Dimensionless
$\rho_w^{in\ situ}(\lambda)$	In situ water reflectance	Dimensionless
$\rho_w^{vic}(\lambda)$	Water reflectance after vicarious adjustment	Dimensionless
$t\rho_g(\lambda)$	Glint reflectance at TOA level	Dimensionless
$t\rho_{wC2(\lambda)}$	TOA water reflectance retrieved by the Bright Pixel Atmospheric Correction at 709, 779, 865 and 885 nm	Dimensionless
$t\rho_w^{pw}(\lambda)$	Pure seawater reflectance at TOA level	Dimensionless
θ_s	Sun zenith angle	Degree
θ_v	View zenith angle	Degree

$\Delta\varphi$	Relative azimuth angle	Degree

2 Motivation to implement a vicarious adjustment

2.1 Theoretical limitation of the instrumental calibration

The primary aim of Ocean Colour Radiometry (OCR) space born sensors such as MERIS is to retrieve the water signal at sea level from a Top Of Atmosphere (TOA) optical measurement, over the Visible (VIS) and Near-InfraRed (NIR) spectral domain.

The signal at ocean surface can be either expressed in term of radiance (energy) $L_w(\lambda)$ or reflectance (ratio to downwelling Solar irradiance) $\rho_w(\lambda)$, where λ is the wavelength. Hereinafter, we shall only consider the water reflectance ρ_w notation, used in the MERIS data distribution context since 2002 (Rast and Bezy 1999) and used more recently for MODIS and SeaWiFS (see *e.g.* http://oceancolor.gsfc.nasa.gov/REPROCESSING/R2009).

The expected accuracy on $\rho_w(\lambda)$ is mainly governed by further exploitation of the signal, for instance to assess marine constituents concentration or other bio-optical quantities (*e.g.* chlorophyll-a, suspended matter, diffuse attenuation coefficient, transparency, etc.) by spectral inversion. In this document we shall rely on the only few specifications derived in the past, essentially designed for quantifying chlorophyll-a in the open ocean. A typical order of relative accuracy is 5% in the blue-green spectral region (Gordon 1997). More recently, for the MERIS mission, the goal of discriminating ten classes of chlorophyll concentration within each of the three orders of magnitude between 0.03, 0.3, 3 and 30 mg/m^3 lead to a requirement of about ±1-2.10^{-3} absolute accuracy at 443 nm and ±5.10^{-4} at 560 nm, using a band ratio algorithm (Antoine and Morel 1999).

Actual accuracy of remotely-sensed ρ_w depends mainly on the quality of both TOA acquisition (*i.e.* quality of the absolute and interband sensor calibration) and the atmospheric correction (*i.e.* ability to estimate and remove the atmospheric path contribution, see *e.g.* Antoine and Morel 1998). This can be made explicit by the following schematic decomposition of the signal, in ideal conditions without sun specular reflection or white caps, and after correction of atmospheric gas absorption (see symbols definition in § 1.3):

$$\rho_{gc}(\lambda) = \rho_{path}(\lambda) + t_d(\lambda).\rho_w(\lambda) \qquad (1)$$

The ρ_{gc} quantity will be described more precisely latter in the MERIS context, and can be understood, at this stage, as the TOA reflectance ρ_{TOA} processed up to the atmospheric correction.

Most of the current operational atmospheric correction algorithms consist in first, assessing the aerosol optical properties from the NIR bands; then, propagating the path reflectance $\rho_{path}(\lambda)$ and total transmittance $t_d(\lambda)$ at any wavelength λ in the visible; and finally, deducing the marine signal by inversing equation (1) (see Antoine and Morel 1999 for MERIS and Gordon and Wang 1994 for SeaWiFS). Hence, whatever the accuracy of the path

reflectance retrieval, any error $\Delta\rho_{gc}$ on the total signal implies an error $\Delta\rho_w$ on the marine reflectance of:

$$\frac{\Delta\rho_w(\lambda)}{\rho_w(\lambda)} = \frac{\Delta\rho_{gc}(\lambda)}{\rho_{gc}(\lambda)} \Big/ \frac{t_d(\lambda)\rho_w(\lambda)}{\rho_{gc}(\lambda)} \qquad (2)$$

The denominator on the right-hand side represents the relative contribution of the marine reflectance at TOA level to the total signal and typically lies between 5% and 20%, depending on the wavelengths and clarity of the water (see figure below). This means that reaching a 5% accuracy on ρ_w requires an absolute accuracy on ρ_{gc} (hence on ρ_{TOA}) between 0.25% and 1%, which cannot be insured through purely instrumental calibration and characterisation (Gordon 1998).

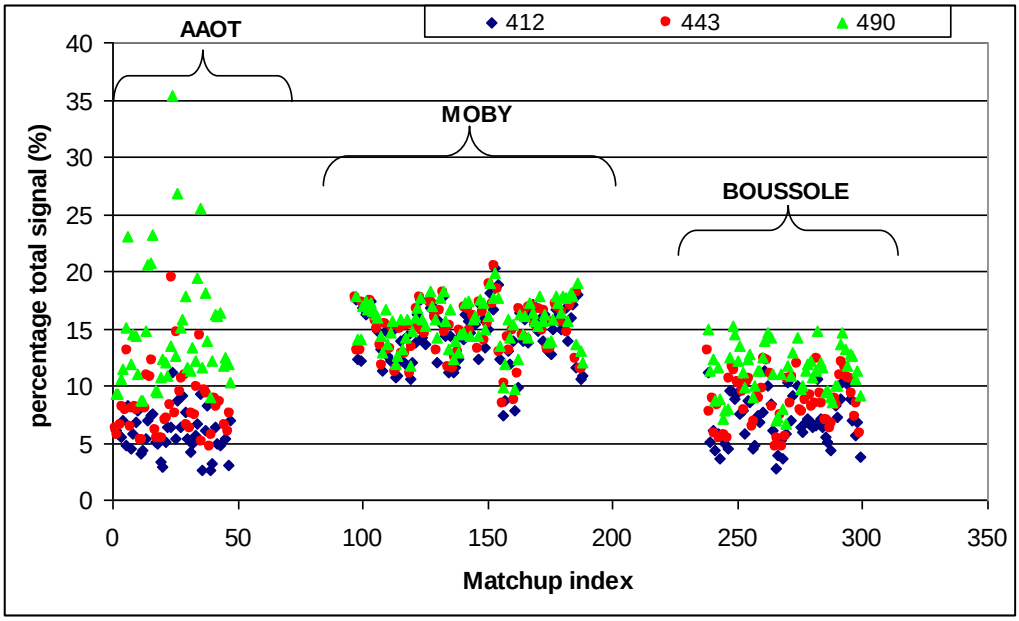

Figure 1: Example of relative contribution of the marine signal to the total signal, $t_d(\lambda)\rho_w(\lambda)/\rho_{gc}(\lambda)$, for MERIS acquisitions over different type of waters: AAOT (Adriatic Sea), MOBY (Pacific Ocean) and BOUSSOLE (Mediterranean Sea).

For instance, the first results for the MERIS calibration and validation showed that the *in situ* estimations of TOA radiances lay within less than 6% of the MERIS measurement (Kneubühler, 2002). Regarding SeaWiFS, pre-launch calibration uncertainties are approximately 3% of the TOA radiance (Eplee *et al.*, 2001).

2.2 MERIS OCR quality assessement of the 2nd reprocessing

Several independent validation exercises conducted in the last years have given evidence for a significant positive bias in the MERIS water reflectance. For instance, Antoine *et al.* 2008 have quantified over the BOUSSOLE buoy a relative percentage difference of about 60% at

412 nm, 30% at 443 nm, 15% at 490 nm and 20% at 510 and 560 nm. Zibordi *et al.* 2006 *also* found values between 15% and 42% in the 443-560 nm spectral range at the AAOT site.

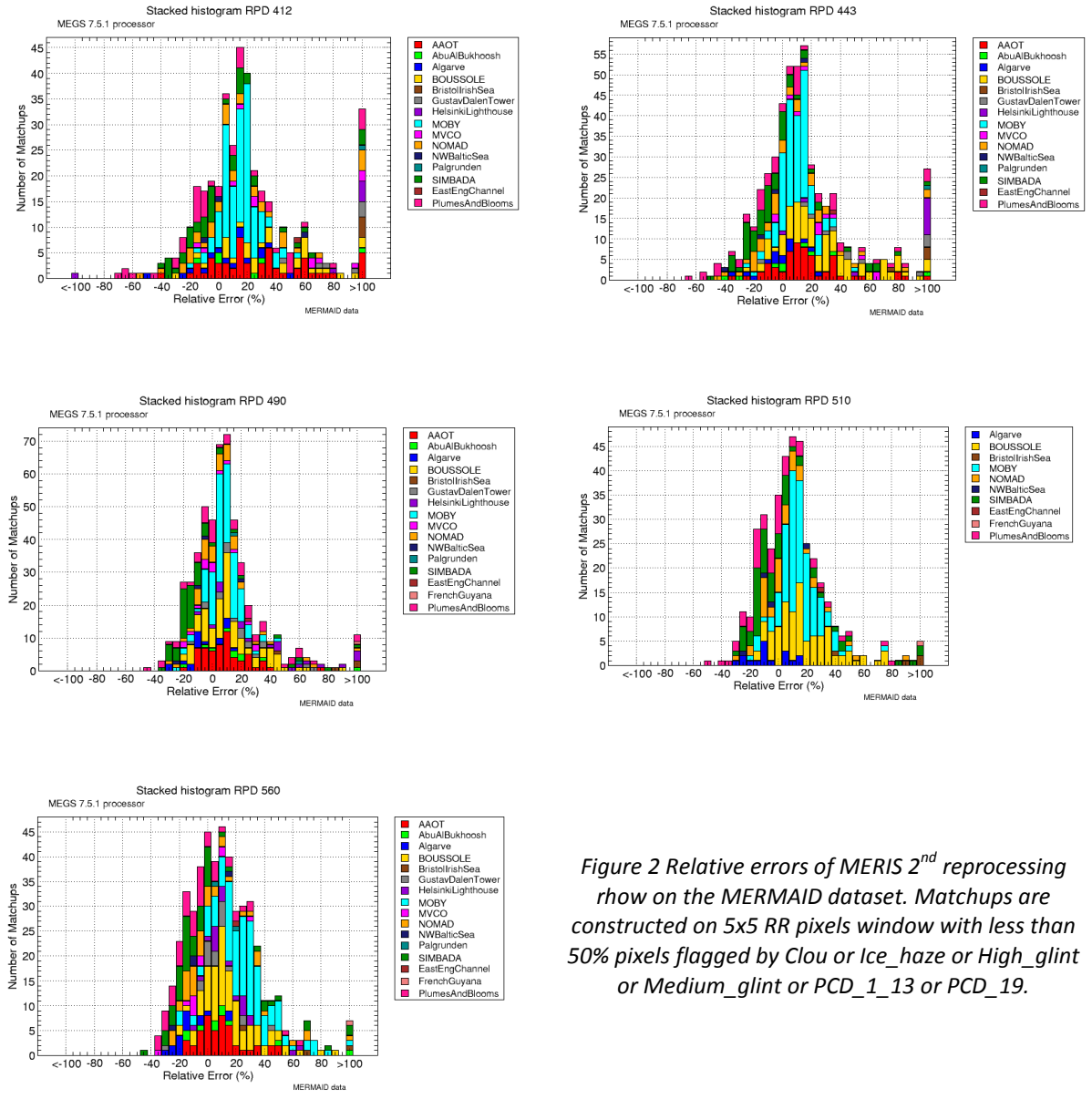

Figure 2 Relative errors of MERIS 2nd reprocessing rhow on the MERMAID dataset. Matchups are constructed on 5x5 RR pixels window with less than 50% pixels flagged by Clou or Ice_haze or High_glint or Medium_glint or PCD_1_13 or PCD_19.

More recently, the MERMAID matchup system has been set up in collaboration with *in situ* data providers in order to get a significant number of validation points with controlled quality. It constitutes a central tool in the present work, with more than 20 *in situ* datasets (fixed stations or cruises, including the NOMAD dataset described in Werdell and Bailey 2005) associated to MERIS data extractions. Details on the optical measurements protocols and matchup facility are available on the website http://hermes.acri.fr/mermaid. The quality assessment of the MERIS 2nd reprocessing on the MERMAID matchups confirms globally a large overestimation in the water reflectance, of few tens of percent (see histograms below).

It is especially true for clear or moderately turbid waters (MOBY, BOUSSOLE, AAOT), while more turbid waters (part of the SIMBADA cruise, Plumes & Blooms…) show negative bias. This difference between both kinds of waters may come from the atmospheric correction over bright pixels in the NIR and will necessitate a distinction in the coming analysis.

Matching the required 5% uncertainty on the water radiometry is thus not met with the standard MERIS processing, and, more generally, is agreed to be particularly difficult for any sensor (see *e.g.* Hooker *et al* 1992, Hooker and McClain 2000 for SeaWiFS). This has lead NASA to rely on vicarious calibration for SeaWiFS and MODIS, that is on a complementary calibration using ground-truth measurements (see Franz *et al.* 2001, Franz *et al.* 2007; Bailey *et al.* 2008 for recent methodologies and results).

Following the recommendation of works cited above, the MERIS Quality Working has decided to consider a vicarious methodology for the 3rd MERIS reprocessing, detailed on the remainder of this document.

2.3 Principle of the adjustment for MERIS

In this document it is chosen to use the terminology of a vicarious *adjustment*, rather than *calibration* as in the seminal work on the NASA sensors (*e.g.* Gordon 1997, Franz *et al.* 2001), because our purpose is to adjust internally the Level 2 Ocean branch processing and not to modify the Level 1 TOA radiometric calibration. Hence it is worth noting that the Level 1 products of the 3rd MERIS reprocessing are not vicariously adjusted.

The primary idea of the vicarious adjustment is to consider that errors in water reflectance come from a systematic bias at TOA, which can be assessed by comparison to reference or *targeted* reflectance ρ_{gc}^{t} on a trustworthy dataset of *in situ* observations. We recall here that ρ_{gc} is equivalent to ρ_{TOA} after some pre-corrections and outside the sun glint (or after correction for it). This problem might come either from an actual bias in the radiometric calibration of the sensor or from inaccuracy of the atmospheric correction based on a radiative transfer modelling. The vicarious adjustment aims at solving blindly the bias issue whatever its exact origin.

For a given target in space and time, hereafter indexed by *i*, the comparison between the ground truth signal ρ_{gc}^{t} and the measured reflectance ρ_{gc} leads to a local adjustment factor defined by:

$$g(\lambda, i) = \frac{\rho_{gc}^{t}(\lambda, i)}{\rho_{gc}(\lambda, i)} \qquad (3)$$

Provided a statistically representative amount of targets, N, and homogeneous individual factors $g(\lambda, i)$, a reliable average gain can then be calculated by:

$$\bar{g}(\lambda) = \frac{\sum_{i=1}^{N} g(\lambda, i)}{N} \qquad (4)$$

Once determined, this gain is systematically applied in operation as a multiplicative factor to the measured TOA reflectance $\rho_{gc}(\lambda)$, just before the atmospheric correction step.

It is important to notice that a single set of spectral gains is applied throughout the entire mission and whatever the camera and CCD detector in the field of view. Hence homogeneity in the individual factors $g(\lambda, i)$ should ensure a robust vicarious calibration.

The targeted reflectance ρ_{gc}^{t} required in the gain computation would ideally be built from concommitant ground measurements of water reflectance, atmospheric aerosol reflectance and atmospheric total transmittance. While reliable *in situ* water reflectances $\rho_w^{in\ situ}$ are accessible, simultaneous measurements with aerosol properties are not widely available (Franz *et al.*, 2001). To remedy this lack of *in situ* measurements, published procedures have proposed to use the atmospheric variables determined algorithmically by the atmospheric correction above the marine target, after insuring a proper calibration of the NIR bands (Franz *et al.* 2007, Bailey *et al* 2008). This implies a two-step procedure:

1. First, the NIR bands used in the atmospheric correction, 779 and 865 nm, are independently adjusted, if necessary;
2. Then, the atmospheric correction is applied, yielding to path reflectance and transmittance in the VIS bands considered as sufficiently accurate to build the targeted TOA reflectance:

$$\rho_{gc}^{t}(\lambda, i) = \rho_{path}^{vic}(\lambda, i) + t_d^{vic}(\lambda, i)\rho_w^{in\ situ}(\lambda, i) \qquad (5)$$

where the exponent ^{vic} stands for vicariously adjusted quantities.

An advantage of this approach, pointed out in the first works of NASA, is to decouple the NIR and VIS gains computations and avoid a complex iterative procedure.

Without further atmospheric *in situ* measurement, the first step needs assumptions on the aerosol signal in the NIR. This can be either by fixing an aerosol model already tabulated in the ground segment (*e.g.* Franz *et al.* 2007), or by making an assumption on the spectral shape as proposed hereafter.

By construction, applying the individual gain $g(\lambda, i)$ would locally make the atmospheric correction perfectly retrieve the desired *in situ* reflectance $\rho_w^{in\ situ}(\lambda, i)$, whatever the NIR adjustment. This is not true in practice since only an averaged adjustment factor $\bar{g}(\lambda)$ is applied. Hopefully the near infrared adjustment may tend to improve accuracy of the atmospheric correction and consequently reduce dispersion in the visible gain factors.

2.4 Domain of applicability

The primary unknown in $\rho_{gc}^{t}(\lambda)$ being the water reflectance and the aerosol reflectance (see *e.g.* equation 5), we have decided to limit ourselves to situations of stable and homogeneous

marine and aerosol properties, *i.e.* avoid coastal areas to minimize the influence of highly variable and complex waters and aerosol assemblages.

In addition, and despite the importance of monitoring coastal regions, the objective of vicarious adjustment is to improve remote-sensing of the widest possible areas of the oceans: open ocean areas dominated by phytoplankton optical properties. For these reasons, the computation of the vicarious adjustment gains has been performed on clear oceanic waters. The application of those gains will obviously present some limitations in coastal waters, discussed hereafter.

3 Algorithm overview

3.1 Reminder of the MERIS Level 2 chain

For the sake of completeness, we give here an overview of the Level 2 processing chain and detail where the vicarious adjustment has been inserted. An overall sketch is provided in Figure 3. Depence on the geometrical angles θ_s, θ_v and $\Delta\varphi$ is not made explicit.

MERIS Level 1 products correspond to geolocated and calibrated TOA radiances $\mathrm{L_{TOA}}$. The Level 2 chain starts by converting the Level 1 data into TOA reflectances ρ_{TOA}. Then, several processings are sequentially applied, pixel by pixel: a pixel identification which allows to flag Cloud, Water and Land pixels; a correction of gaseous absorption for O3, O3 and H20; the smile effect correction in order to reduce the in-field of view variation of channels central wavelengths. At this stage the corrected reflectances, internally noted ρ^*_{ng}, can be modelled for the water pixels by:

$$\rho^*_{ng}(\lambda) = \mathrm{t}\rho_g(\lambda) + \rho_{path}(\lambda) + t_d(\lambda)\rho_w(\lambda) \qquad (6)$$

where $\mathrm{t}\rho_g$ is the glint reflectance at TOA. This latter is estimated at sea level by the Cox and Munck 1954 model with parametrization from Ebuchi and Kizu 2002 and propagated at TOA by a simplified transmittance (see MERIS ATBD 2.13). Note that there is currently no white-caps modelling in the MERIS processing. The glint corrected reflectance, $\rho_{gc}(\lambda)$, then enters the atmospheric correction step, whose goal is to decouple the marine and atmospheric signals:

$$\rho_{gc}(\lambda) = \rho_{path}(\lambda) + t_d(\lambda)\rho_w(\lambda) \qquad (7)$$

Once the spectrum $\rho_w(\lambda)$ retrieved, the further steps of the Level 2 chain deal with bio-optical inversion to compute concentration of marine species; these downstream steps are out of scope of this document.

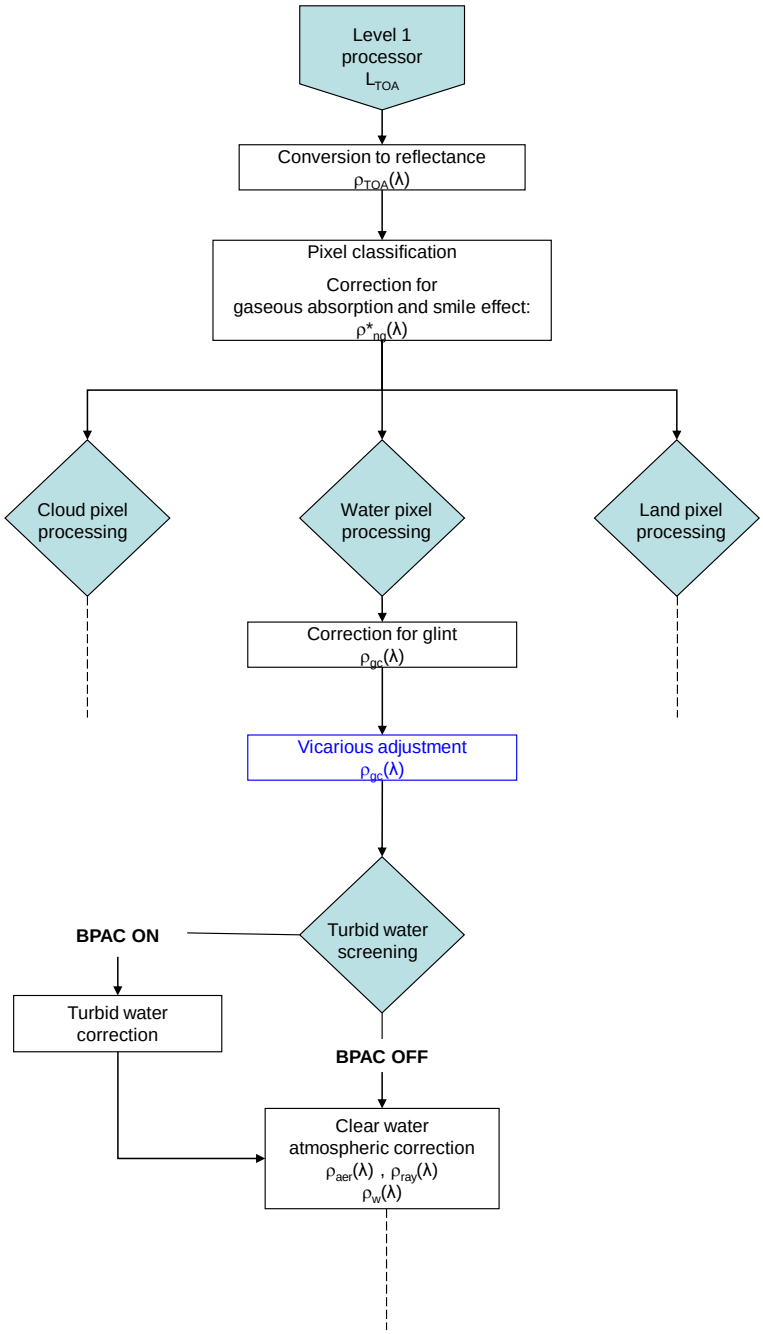

Figure 3: Flow diagram of MERIS level 2 processing (limited to ocean color radiometry)

3.2 The atmospheric correction

In order to understand the vicarious adjustment process in detail, and in particular the distinction between NIR and VIS adjustment, it is necessary to review the components of the atmospheric correction. The algorithm is a two-step approach launched indistinctly on all water pixels.

First, the Bright Pixel Atmospheric Correction (BPAC, Moore and Lavender 2011) identifies any residual marine signal in the NIR bands due to backscattering of sediments or coccoliths. An iterative procedure inverse a coupled bio-optical and atmospheric model at 709, 779, 865 and 885 nm, parameterized by the absorption and backscattering coefficient of particles, as well as aerosol reflectance. The single scattering approximation is used to decouple the Rayleigh and aerosol reflectance. In practice, the BPAC retrieves a TOA marine signal $t\rho_{wC2}(\lambda)$ which searches to satisfy the following modeling in the four NIR bands:

$$t\rho_{wC2}(\lambda) = \rho_{gc}(\lambda) - \rho_R(\lambda) - \rho_{aer}(\lambda_{865})\left(\frac{\lambda}{\lambda_{865}}\right)^{\varepsilon} \qquad (8)$$

where $\rho_R(\lambda)$ is the Rayleigh reflectance, computed from tabulated radiative transfer simulations and $\rho_{aer}(\lambda_{865})$ and ε are respectively the aerosol reflectance and spectral slope retrieved by the BPAC.

In case of a failure in the inversion, the $t\rho_{wC2}(\lambda)$signal is simply set to the reflectance of pure sea water. This happens in particular for very clear waters, where too low values associated to instrinc noise of the measurement cannot allow convergence.

Second, the Clear Water Atmospheric Correction (Antoine and Morel 1999, Antoine and Morel 2011) uses two bands in the NIR, namely 779 and 865 nm, to determine the two unknowns of the path reflectance: amount and type of aerosols. The path reflectance in the NIR is estimated by removing the turbid signal to the TOA signal, allowing to recover the *black pixel* assumption:

$$\rho_{path}(\lambda_{NIR}) = \rho_{gc}(\lambda_{NIR}) - t\rho_{wC2}(\lambda_{NIR}) \qquad (9)$$

The method makes use of Look-up tables (LUT) relating theoretical ρ_{path}/ρ_R ratio to the aerosol optical thickness, for a set of aerosol models. These LUTs are generated by radiative transfer simulation taking into account multiple scattering between aerosol and molecules (Antoine and Morel 1999). Schematically, the algorithm identifies the aerosol optical thickness at 865 nm and the two models that best bracket the actual ρ_{path}/ρ_R ratio at 779 and 865 nm; furthermore it computes a mixing ratio, which can be seen as the interpolation coefficient between the two tabulated models. Once these aerosol properties are retrieved in the NIR, the path reflectance can be computed at any wavelength, as well as the total transmittance $t_d(\lambda)$ (upward and downward) thanks again to LUTs generated by radiative

transfer simulation for the same set of aerosol models. The water reflectance can then be deduced by

$$\rho_w(\lambda) = \left(\rho_{gc}(\lambda) - \rho_{path}(\lambda)\right)/t_d(\lambda) \qquad (10)$$

It is important to notice that the aerosol retrieval, although based on accurate ρ_{path}/ρ_R LUTs, strongly depends on the single scattering approximation in the NIR through equation (9) and (8).

3.3 Vicarious adjustment implementation

As already explained in the introduction and through equation (2), any error on $\rho_{gc}(\lambda)$ directly impacts the water reflectance at the wavelength λ. The inherent approximations and algorithmic limitations of atmospheric correction itself, which uses ρ_{gc} in the NIR to determine and propagate ρ_{path} along the full spectrum, also might produces error on ρ_w. This justifies to adjust this precise quantity rather than the TOA Level 1 signal.

In the Level 2 processor, the vicarious adjustment is thus simply implemented by multiplying $\rho_{gc}(\lambda)$ by the gain factors, just before the atmospheric correction (see also Figure 3):

$$\rho_{gc}^{vic}(\lambda) = \bar{g}(\lambda)\rho_{gc}(\lambda) \qquad \text{for all } \lambda \qquad (11)$$

This apparent simplicity hides the most difficult part of the exercise which consists in computing a reliable set of factors $\bar{g}(\lambda)$. This is the purpose of the remaining part of the document.

There is no other algorithmic change in the Level2 chain, but the adjustment has two effects:

- Firstly the adjustment in the NIR modifies the aerosol selection, yielding to new path reflectance ρ_{path}^{vic} and transmittance t_d^{vic};
- Secondly, the adjustment in the visible also impacts directly the marine reflectance by

$$\rho_w(\lambda) = \left(\bar{g}(\lambda)\rho_{gc}(\lambda) - \rho_{path}^{vic}(\lambda)\right)/t_d^{vic}(\lambda) \qquad (12)$$

The question of applying the multiplicative gains before the glint correction has been considered. The relative difference at TOA level between both approaches would be equal to $\frac{\Delta\rho_{gc}(\lambda)}{\rho_{gc}(\lambda)} = (\bar{g}(\lambda) - 1)\frac{t\rho_g(\lambda)}{\rho_{gc}(\lambda)}$ which has been estimated, thanks to figures of $\bar{g}(\lambda)$ presented hereafter and realistic $t\rho_g$ values, of the order of less than 0.1%. The impact would thus be lower than the expected accuracy. Finally, applying the gain at the entry of the atmospheric correction allows a comprehensible study of the adjustment without other source of uncertainties in the modelling.

4 Algorithm description

This section describes in detail the gain computation and validation of the vicarious adjustment on matchups and on global Level 3 analysis.

4.1 Theoretical description

Adjusting the NIR band is a prerequisite in order to get reliable path reflectance, to be used in the construction of the reference dataset for VIS gain computation (see equation 5). Adjustments in the two parts of the spectrum are thus described sequentially hereafter.

4.1.1 Adjustment in the NIR

4.1.1.1 Theoretical shape of the path reflectance

There are several ways for considering the issue of NIR radiometric calibration and accuracy. Relying on *in situ* data is a difficult task because there are currently no available measurements of the path reflectance at MERIS overpass, but only optical thickness; furthermore atmospheric measurements, as provided for instance by the AERONET facilities (Holben *et al* 1998), are generally above coastal waters and thus would need a model to take into account the marine signal in the NIR. Associated uncertainties would be by far too big. Instead, previous works (*e.g.* Franz *et al* 2007) have proposed to rely only on the remote-sensed data itself, over oligotrophic sites where the marine signal can be neglected or is properly known. This approach assumes that the NIR path reflectance follows a theoretical spectral shape and that at a reference channel is well calibrated for providing the absolute level of the signal.

The theoretical shape chosen in the NASA approach corresponds to the tabulated path reflectance used in the atmospheric correction, for a given aerosol model. The weakness of this method is thus to fix an aerosol model once for all in the vicarious gain computation. Instead, the method implemented here is based on the single scattering approximation (SSA) in the NIR, which decouples the Rayleigh from the aerosol reflectance, the latter being analyticaly modelled with a supplementary degree of freedom, ε, for its spectral dependence:

$$\rho_{path}(\lambda) = \rho_R(\lambda) + \rho_{aer}(\lambda_{ref})\left(\frac{\lambda}{\lambda_{ref}}\right)^{\varepsilon} \qquad (14)$$

Another reason to choose such a formulation for MERIS is that it is perfectly consistent with the BPAC (see equation 8), whose final effect is to fit the path reflectance in the NIR on the SSA (equation 9). A direct drawback, however, is that we need a second reference channel in order to compute the ε exponent.

To summarise, the theoretical shape to be used in our NIR vicarious adjustment is based on the following assumptions:

- The marine reflectance can be modelled by tabulated value of pure seawater reflectance $\rho_w^{pw}(\lambda_{NIR})$;
- Observation conditions allow to trust the SSA, *i.e.* limited to NIR bands;
- Two NIR channels do not need to be adjusted.

The theoretical (or targeted) TOA reflectance is thus modelled by:

$$\rho_{gc}^{t}(\lambda) = \rho_R(\lambda) + \rho_{aer}(\lambda_{ref})\left(\frac{\lambda}{\lambda_{ref}}\right)^{\varepsilon} + t\rho_w^{pw}(\lambda) \qquad (15)$$

where $\rho_{aer}(\lambda_{ref})$ and ε are two degrees of freedom of the adjustment. The pure seawater reflectance is approximated at TOA ($t\rho_w^{pw}$) by a pure Rayleigh transmittance.

4.1.1.2 Dataset for analysis

Since the adjustment of NIR and VIS bands can be handled separately, their respective datasets do not need to coincide. We here rely on the choice of Franz *et al* 2007, which focuses on two sites in the Southern Hemisphere suitable for NIR vicarious adjustment: the South Indian Ocean (SIO, centered at 20.0° South, 80.0° East) and South Pacific Gyre (SPG, centered at 27.0° South, 134° West).

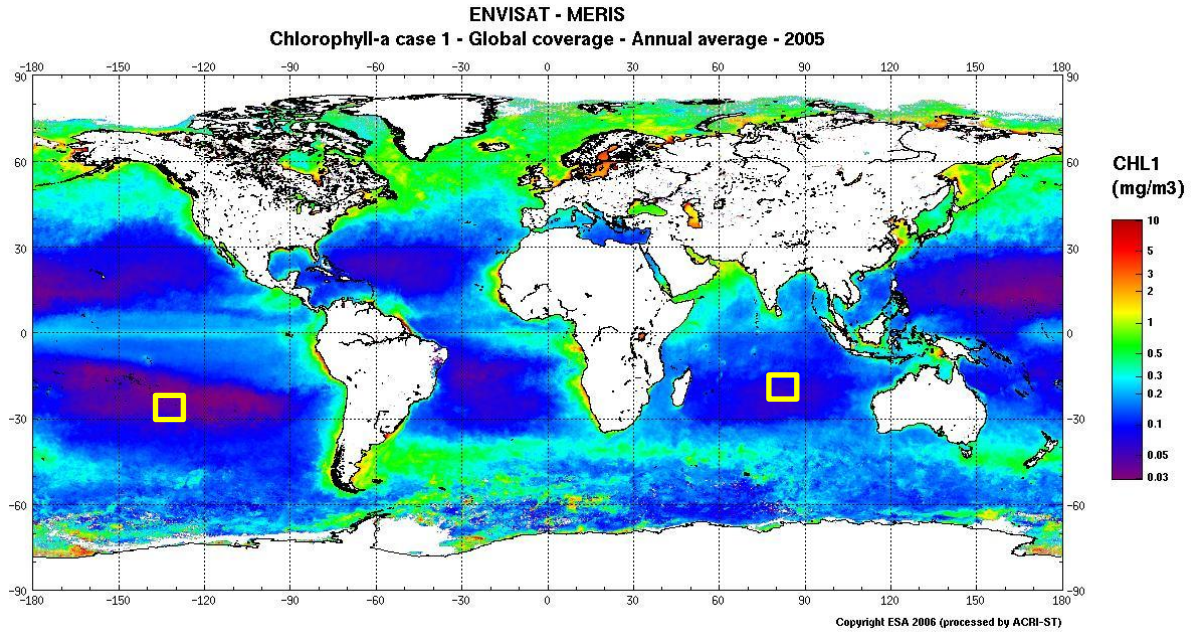

Figure 4: MERIS averaged Chlorophyll-a in 2005 and SPG (left square) and SIO (right square) approximated position.

These two sites have been selected for the following reasons:

- These areas are far away from land and/or active volcanic Islands. The aerosol composition is therefore purely maritime (*i.e.* influenced by sea salt and water vapour).
- They are among the clearest water on Earth with very low level of chlorophyll and sediment concentration which is a condition of validity for the assumption of pure seawater reflectance (equation 15).

We gathered all MERIS tracks overpassing a 10x10 degree box centred on these coordinates from 2003 to 2009, which made a total of 2370 and 2229 images for SIO and SPG respectively, that we processed at Level 1 and Level 2.

We then extracted MERIS data on the best possible area fulfilling our assumptions, taking benefit of some spatial flexibility since no *in situ* location is required at this stage. We employed a nested box approach, by successively searching among the 10x10 degree window the interlocked 64x128 and 15x15 pixels boxes with the less possible Cloud, PCD_1_13, High_glint, Medium_glint and Ice_haze flags, keeping eventually the 5x5 central pixels. This procedure has been visually checked and has proven to provide a large and reliable time series of MERIS clear regions over the two oligotrophic sites. Through this procedure, 2193 and 1842 areas have been gathered for SIO and SPG respectively, which represents a remarkably low rejection of less than 20%. After few trials, the final selection for NIR adjustment inspection consisted in keeping the 5x5 pixels whose embedding 15x15 box do not present any of the Cloud, High_glint, Medium_glint or Ice_haze flags.

4.1.1.3 Need for a MERIS NIR adjustment

From the dataset described above, we have inspected the alignment of the actual MERIS TOA reflectance ρ_{gc} on the theoretical shape of (Eq-15), in the red and NIR spectrum range. To this aim we have computed the degree of freedom $\rho_{\mathrm{aer}}(\lambda_{\mathrm{ref}})$ and ε between the fifteen combinations of $\{\lambda_{\mathrm{ref}}, \lambda\}$ among the 665, 681, 709, 753, 779 and 865 nm walengths. Intercomparison of the fifteen $\varepsilon(\lambda, \lambda_{\mathrm{ref}})$ constitutes an indicator of the proper alignement of the bands. We have inspected the 105 possible intercomparisons between all $\varepsilon(\lambda, \lambda_{\mathrm{ref}})$ and report in the figure below some of them to illustrate our findings. Although the plots are generally very scattered and not perfectly aligned on the 1:1 line, it is noticeable that a major discrepancy occurs when then 865 nm band is considered. This is a general conclusion when looking in details all 105 comparisons.

Those results suggest that bands 665, 681, 709, 753 and 779 nm are pretty well adjusted, at least in a relative sense, while 865 nm clearly departs from them. The same trend occurs for the 885 nm (not shown here), a band not explicitly used in the Clear water atmospheric correction, but which plays a role in the upstream BPAC.

Reason for a misalignement of the 865 nm could come from Level 1 processing, in particular the straylight correction. However this aspect has not been inspected in the MERIS 3rd reprocessing. It is thus decided to correct the 865 and 885 nm bands and fix the gain factors to the unity for the 709 and 779 nm bands used in atmospheric correction.

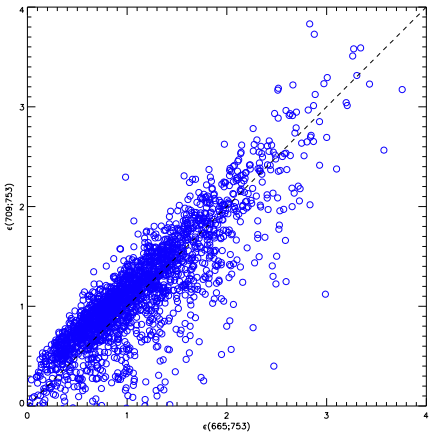

$\varepsilon(709,753)$ vs $\varepsilon(665,753)$

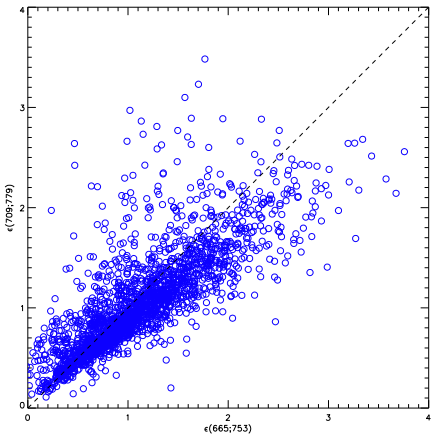

$\varepsilon(709,779)$ vs $\varepsilon(665,753)$

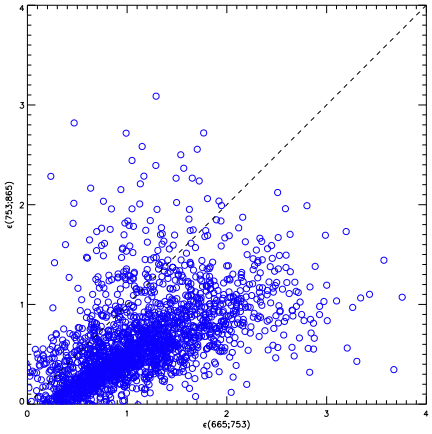

$\varepsilon(753,865)$ vs $\varepsilon(665,753)$

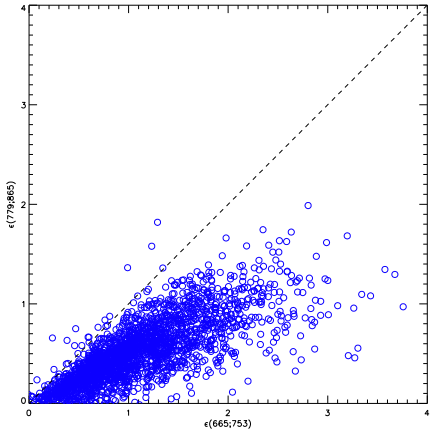

$\varepsilon(779,865)$ vs $\varepsilon(665,753)$

Figure 5: Comparison of the aerosol reflectance spectral dependence, $\varepsilon(\lambda, \lambda_{ref})$, against $\varepsilon(665,753)$ for four $\{\lambda_{ref}, \lambda\}$ couples, including (bottom) or not (top) the 865 nm band. Computation is done on the SIO and SPG extraction dataset.

4.1.1.4 NIR gain time serie and averaged value

Among all possibilities, bands 709 and 779 nm are used as reference to compute ε and $\rho_{aer}(779)$, by a linear resolution on $\log \rho_{aer}(779)$ and ε in equation 15. This choice ensures a clear distinction with the bands considered in the VIS adjustment, while 753 nm is never involved in the MERIS Ocean processing and not further considered here. Computation is done pixel per pixel. Then, the targeted signal at 865 nm deduces by

$$\rho_{gc}^{t}(865) = \rho_R(865) + \rho_{aer}(779)\left(\frac{865}{779}\right)^{\varepsilon} + t\rho_w^{pw}(865) \qquad (16)$$

This yields, for a given pixel *i*, to the vicarious gain at 865 nm:

$$g(865, i) = \frac{\rho_{gc}^{t}(865, i)}{\rho_{gc}(865, i)} \qquad (17)$$

A single gain per scene is finally computed taking the median over the 5x5 box, rejecting pixels with wind speed higher than 9 m/s, chlorophyll-a concentration greated than 0.2 mg/m^3 and aerosol models out of the maritime sets. This latter test, although resulting from the atmospheric correction before the adjustment, is a good criterion to remove undetected atmospheric artifact (haze, cloud shadows…).

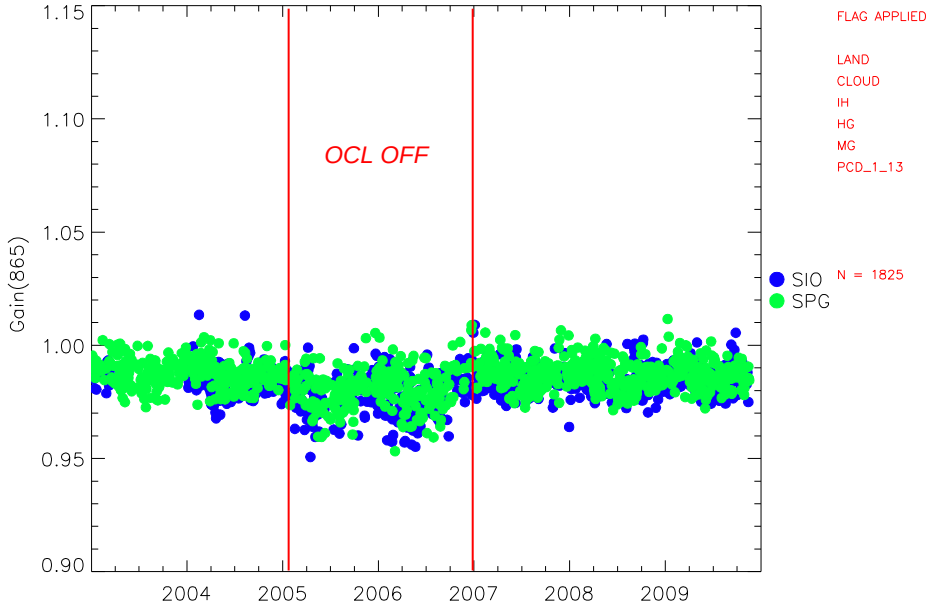

Figure 6: Time series of $g(865)$ at SIO (blue) and SPG (green). The distinctive OCL OFF period (red lines) is rejected to compute average gain.

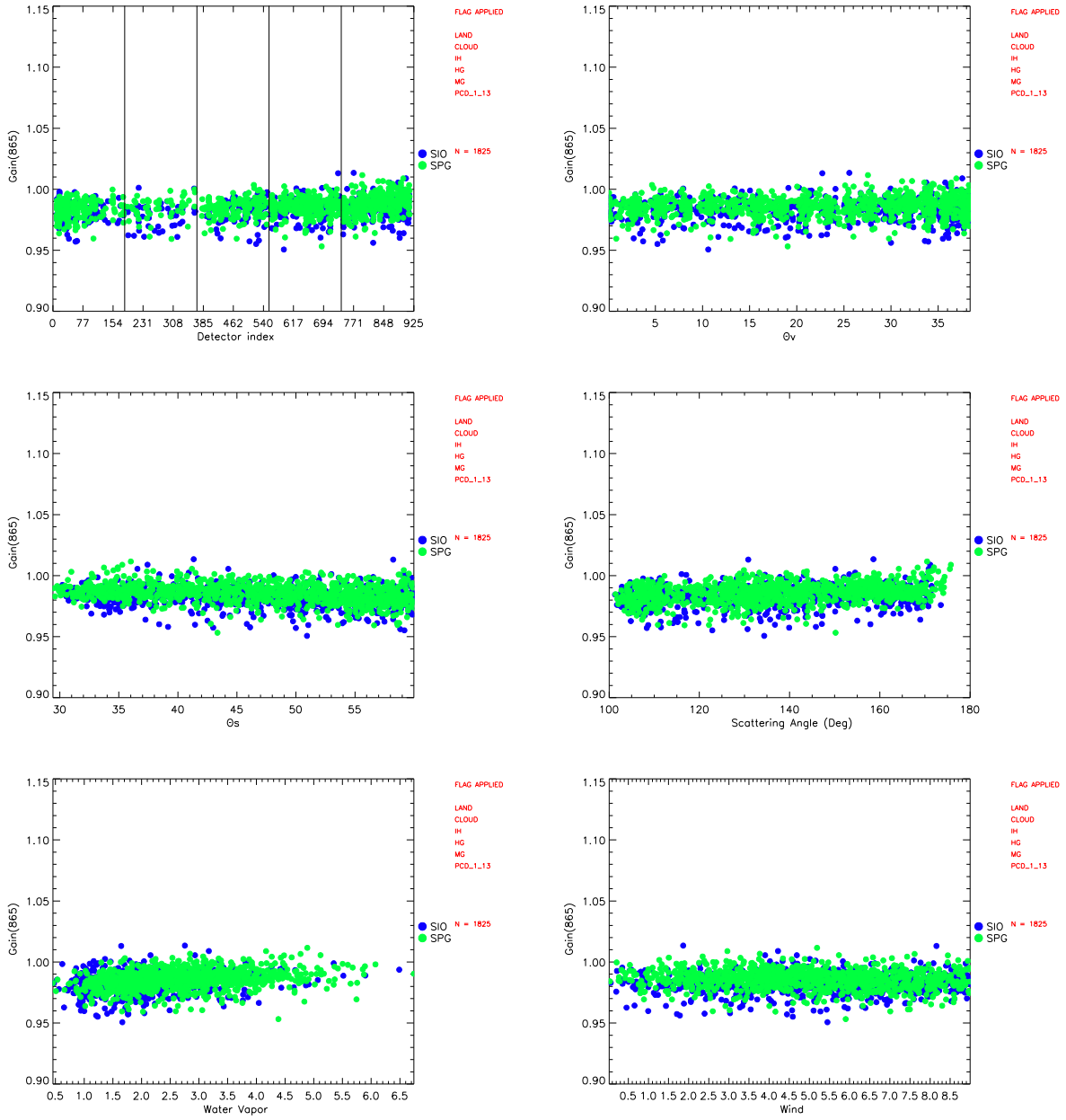

Figure 7: Variation of $g(865)$ at SIO (blue) and SPG (green) from top to bottom and left to right with detector index (vertical lines delimit camera 1 to 5), view zenith angle, sun zenith angle, scattering angle, water vapour and wind modulus

The time serie of $g(865)$ over SPG and SIO is provided in figures above, as well as dependence with respect of detector index, geometry, water vapour and wind speed modulus. These results can be interpreted as follows:

- First, a positive aspect is the very good consistency between both oligotrophic sites, allowing to merge the two datasets in view of a unique averaged gain.
- Second, there is no detectable temporal trend in the gains over the mission life, except, interestingly, a distinctive period from end 2004 to fall 2006. This corresponds

to the temporary onboard de-activation of the Offset Control Loop (OCL) between 13th Decemver 2004 and 9th October 2006; the OCL aims at correcting the dark current and was switched off at that time as a test to avoid small oscillations. A slight seasonal trend is detectable, of however much lower amplitude than using the fixed aerosol approach (see section 4.1.3.2).

- Variation of $g(865)$ along the swath is mainly noticeable through a small number of valid points in camera 2 due to presence of the Sun glint, and in a less extent adjacent camera 1 and 3. The slight parabolic shape along the detector is thus hard to interpret, with a heterogeneous number of points and associated heterogeneous scattering. In addition to that, looking at variation through the viewing zenith angle does not show any trend across track.
- Dependence on sun zenith and scattering angle is very weak, with a slight trend toward high values; this is related to the slight seasonal cycle already mentioned, obviously followed by these two angles.
- Eventually, compared to its intric noise, $g(865)$ appears robust against the water vapour and wind speed.

The averaged adjustment gains are provided in table below. Note that the OCL OFF period is discarded in these final values. The gains represent a correction of about -1.4% at 865 nm and -1.7% à 885 nm. The dispersion is comparable to that published for SeaWiFS (standard deviation at 765 of 0.01 in Franz *et al.* 2007).

Table 1: Gain computed through SSA from 620 up to 885nm

WL (nm)	Gain	Std	N
620	1.0065	0.0070	1339
665	1.00190	0.0048	1339
681	0.9995	0.0044	1339
709	1.		1339
753	1.0033	0.0030	1339
761	1.		1339
779	1.		1339
865	0.9864	0.0064	1339
885	0.9829	0.0102	1339
900	1.		1339

For the sake of completeness, we have also computed the gains at other red and NIR bands inspected previously. Their adjustment is clearly below the one of 865 nm; the highest at 620 nm is twice lower than the one 865 nm, with an identical spectral distance to the reference bands 709 and 779 nm.

The gains at 761 nm and 900 nm are arbitrary set to one, since those bands are not involved in the atmospheric correction and are only used for upstream gaseous correction.

4.1.1.5 Validation of the SSA assumption and error budget

In order to assess the relevance of the SSA assumption, we have applied our adjustment approach on a set of theoretical TOA reflectances and looked whether resulting gains were as close as possible to the unity. The synthetic dataset has been simulated with the MEROS database (Santer and Zagolski 2010), which is based on the Successive Order of Scattering (SOS) radiative transfer code over wind-roughened black sea surfaces. We have started from the SIO and SPG extractions of (θ_s, θ_v, $\Delta\varphi$), surface pressure and wind speed in view of processing an identical number of points to the real adjustment, with equivalent distribution in geometry and meteorological conditions; then we have replaced the actual ρ_{gc} by the associated MEROS simulations, varying randomly and blindly the aerosol models among the 16 MERIS standard models (see Zagolski 2010) and optical thnicknesses (between 0 and 0.35 at 560 nm).

Figure 8 presents the time series of $g(865)$ and the median gains at all wavelengths in the red/NIR. The resulting gains are almost perfecty equal to one (maximum correction at 620 nm of 0.33%) which tends to support the reliability of the gain computation procedure. Figure 9 presents the gains at 865nm versus θs, θv, scattering angle and wind speed; they are globally very robust, despite a bigger dispersion for scattering angles higher than 160°.

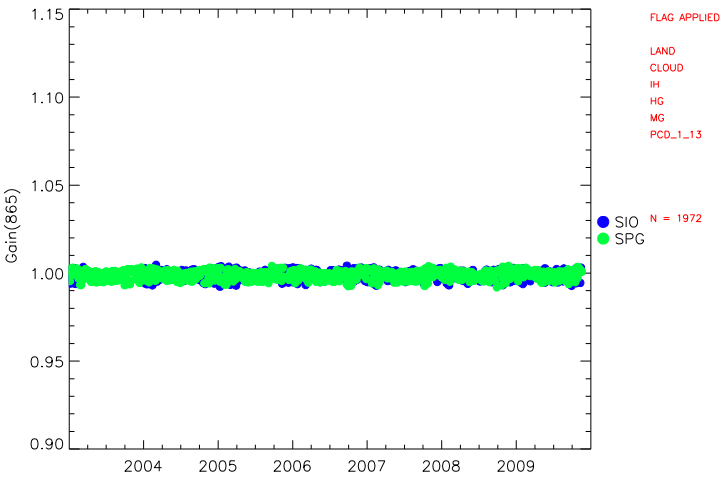

WL (nm)	Gain
620	1.0033
665	1.0013
681	1.0006
709	1.
753	1.0001
779	1.
865	0.9992
885	0.9987

Figure 8: Time series of $g(865)$ on the simulated MEROS spectra, using the SSA approach and averaged gains for all bands in the red/NIR.

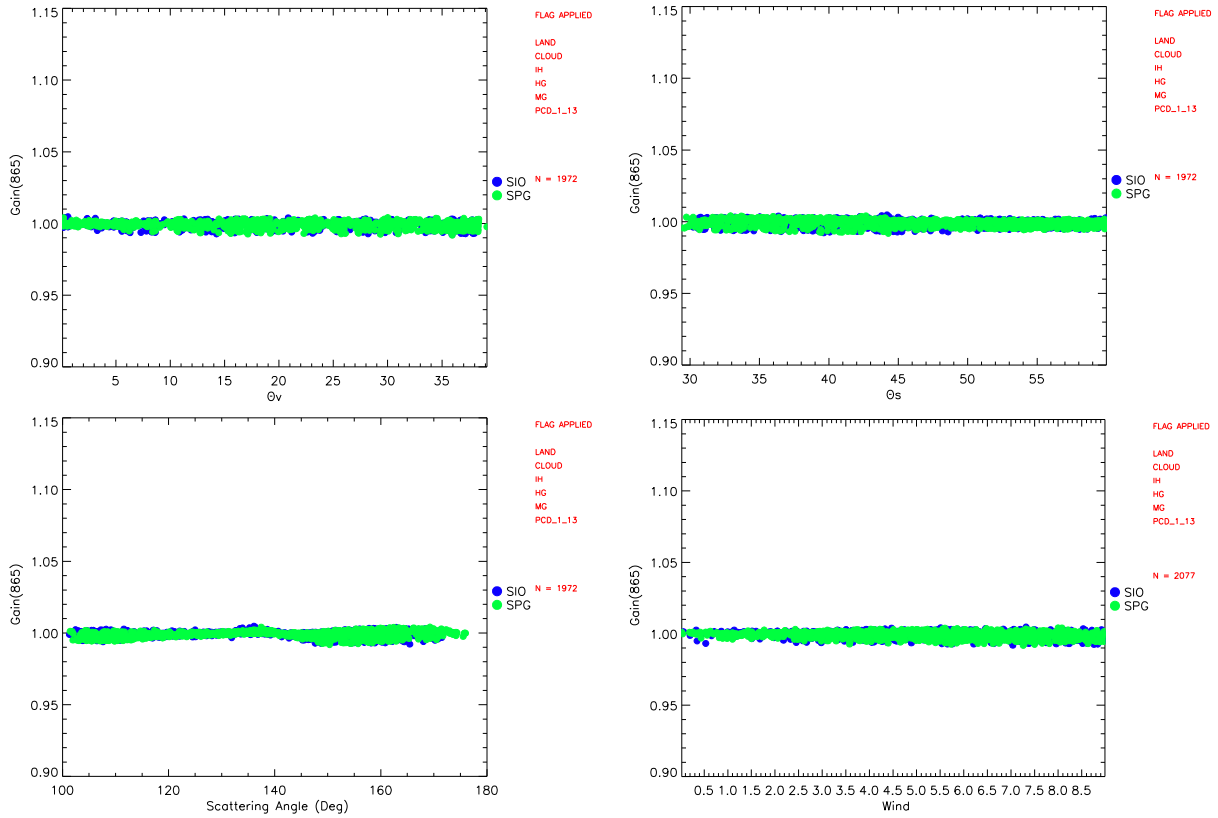

Figure 9: Variation of g(865) on the MEROS simulated spectra with SIO (blue) and SPG (green) conditions of observation, from top to bottom and left to right with respect to view zenith angle, sun zenith angle, scattering angle and wind modulus

Further to this, we have attempted to relate the gains dispersion to the noise in the reference bands. Introducing a Gaussian random error of 1, 2, 3, 4 and 5 % on $\rho_{gc}(779)$ yields a proportional standard deviation at 865 nm up to 5% (see Table 2). In addition, the averaged gains remain almost unchanged. The linear relationship between the standard deviation in $g(865)$ and the relative error in $\rho_{gc}(779)$, depicted in Figure 10, is interesting to come back to the real data: with an actual standard deviation in the gain of about 0.6%, we deduce that the actual noise in $\rho_{gc}(779)$ on the real SIO and SPG dataset should be lower than 1%.

Table 2: Impact of a random error in $\rho_{gc}(779)$ on the calculation of $g(865)$ on the MEROS dataset

WL	nominal		Noise 1%		Noise 2%		Noise 3%		Noise 5%	
620	1.0033	0.0022	1.0035	0.0039	1.0039	0.0068	1.0038	0.0103	1.0051	0.0173
665	1.0013	0.0011	1.0014	0.0021	1.0016	0.0037	1.0015	0.0057	1.0021	0.0094
681	1.0006	0.0006	1.0006	0.0013	1.0007	0.0024	1.0007	0.0037	1.0010	0.0061
709	1.0000	0.0000	1.0000	0.0000	1.0000	0.0000	1.0000		1.0000	0.0000
753	1.0001	0.0005	1.0000	0.0024	0.9998	0.0045	1.0000	0.0070	0.9996	0.0116
779	1.0000	0.0000	1.0000		1.0000		1.0000		1.0000	
865	**0.9992**	**0.0022**	**0.9991**	**0.0098**	**0.9984**	**0.0186**	**0.9997**	**0.0293**	**0.9993**	**0.0492**
885	0.9987	0.0033	0.9986	0.0115	0.9978	0.0216	0.9994	0.0340	0.9992	0.0573

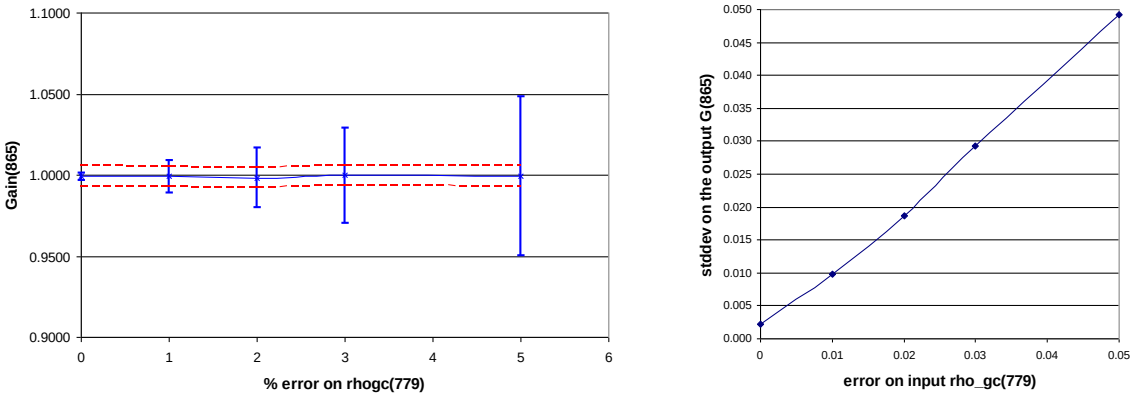

Figure 10: Left: Averaged gain at 865 on the MEROS dataset and associated standard error as a function of the percentage of random error on $\rho_{gc}(779)$. The red line represents the standard deviation of $g(865)$ computed with the real dataset. Right: Standard deviation as a function of the error on input $\rho_{gc}(779)$.

Eventually, we have added a -2% bias on the $\rho_{gc}(865)$ of the simulated dataset, varying again the noise at 779 nm, and checked that the algorithm retrieves a gain close to the expected 1.02 value (see Table 3 and figure Figure 11). The relative error is always below 0.08% and the standard deviation identical to the one computed previously.

In conclusion, all these numbers show that $g(865)$ is computed with accuracy better than 0.1% and precision better than 1%.

Table 3: Impact of a random error in $\rho_{gc}(779)$ and a bias of -2% in $\rho_{gc}(865)$ on the calculation of $g(865)$ on the MEROS dataset

WL	nominal		Noise 1%		Noise 2%		Noise 3%		Noise 5%	
620	1.0033	0.0022	1.0035	0.0040	1.0033	0.0066	1.0036	0.0105	1.0050	0.0203
665	1.0013	0.0011	1.0014	0.0022	1.0013	0.0037	1.0014	0.0058	1.0020	0.0099
681	1.0006	0.0006	1.0006	0.0014	1.0005	0.0024	1.0006	0.0038	1.0009	0.0063
709	1.0000		1.0000		1.0000		1.0000		1.0000	
753	1.0001	0.0005	1.0000	0.0024	1.0002	0.0045	1.0002	0.0072	0.9998	0.0115
779	1.0000		1.0000		1.0000		1.0000		1.0000	
865	**1.0196**	**0.0023**	**1.0191**	**0.0101**	**1.0204**	**0.0197**	**1.0208**	**0.0309**	**1.0203**	**0.0490**
885	0.9987	0.0033	0.9982	0.0116	0.9997	0.0226	1.0003	0.0352	0.9999	0.0559

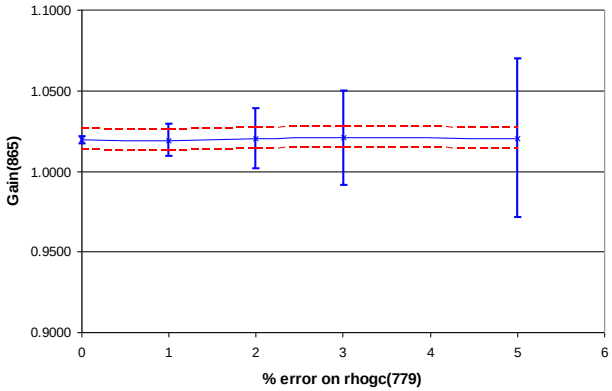

Figure 11: Averaged gain at 865 on the MEROS dataset with a bias of -2% in $\rho_{gc}(865)$ and associated standard error as a function of the percentage of random error on $\rho_{gc}(779)$. The red line represents the standard deviation of $g(865)$ computed with the real dataset.

4.1.1.6 Impact on clear waters

Although it does not directly concern the TOA signal in the visible, the NIR adjustment impacts the water reflectance in the blue/green bands by modifying the path reflectance of the atmospheric correction. It is interesting to assess this effect on its own, as a validation of the approach, on matchups that were not used in the NIR gain computation. We have here restricted the analysis to the BOUSSOLE, MOBY and NOMAD datasets. More details on those *in situ* measurements will be given in the next section.

We have launched two configurations of the 3rd reprocessing processor (MEGS8): without any vicarious adjustment, and with the NIR adjustment presented previously. The matchups are built on 5x5 RR pixels, with a time difference lower than 3 hours and less than 50% of the pixels being Land or Cloud or Ice_haze or Medium_glint or High_glint or PCD_1_13.

The scatter plots of ρ_w and histograms of relative errors, displayed from Figure 12 to Figure 15 below, shows a very satisfying impact of the NIR adjustment. The regression line gets closer to the 1:1 line at all wavelengths (in particular at 665 nm), although around 7% of points becomes invalid.

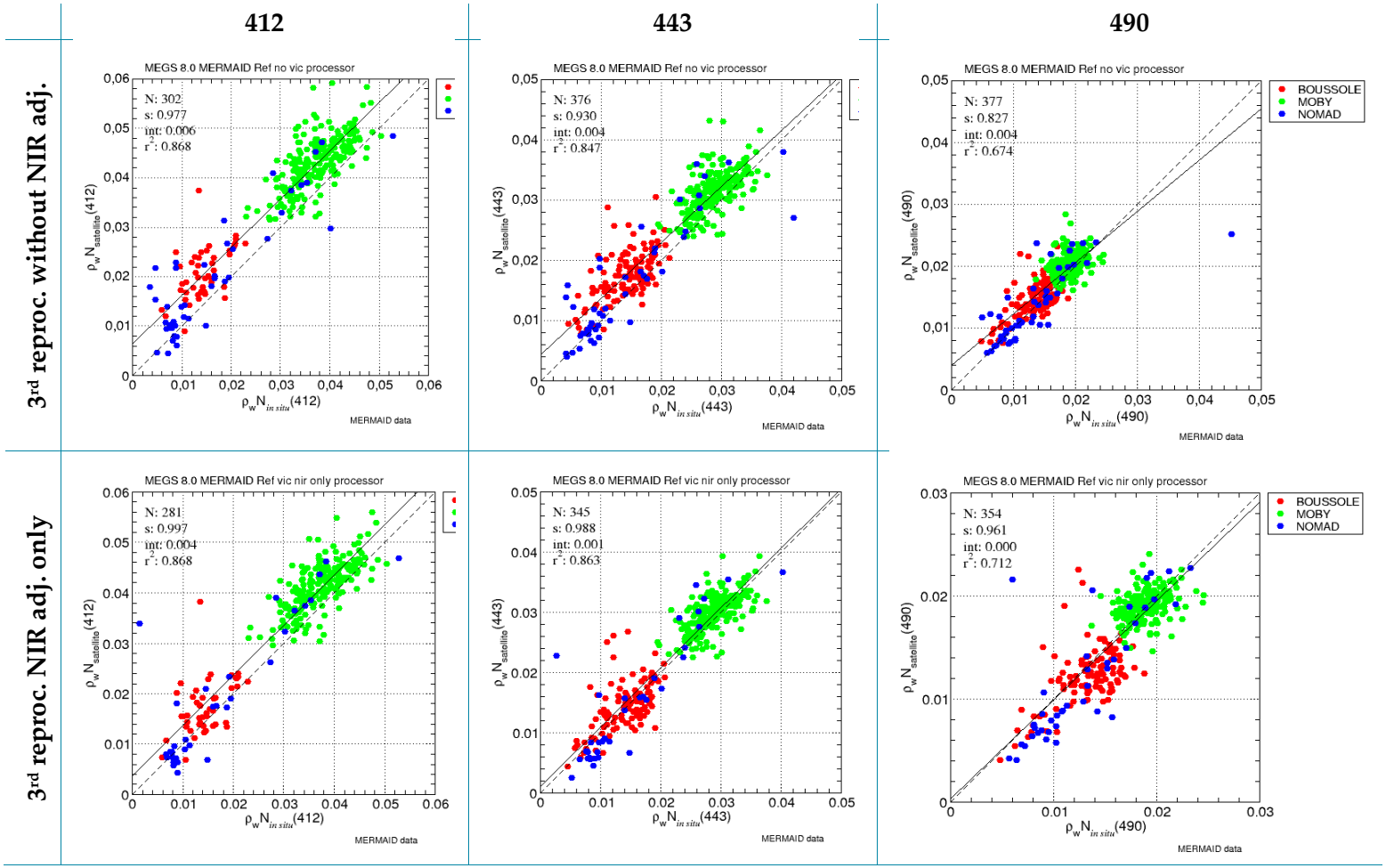

Figure 12: 3rd reprocessing ρ_w without NIR adj. (top) and with NIR adjustment (bottom) versus in situ data (MERMAID clear waterdataset - bands 412, 443, 490)

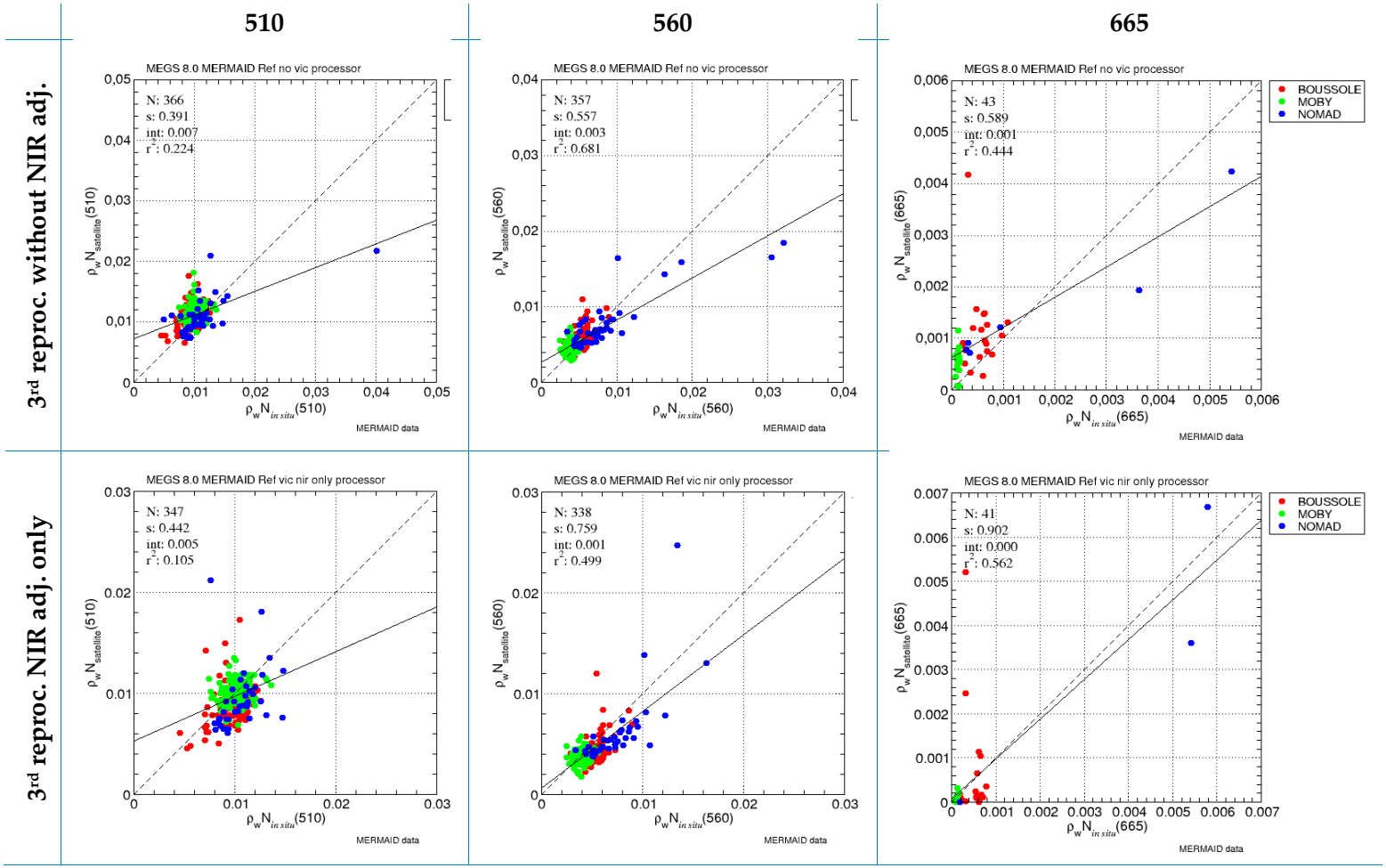

Figure 13: 3rd reprocessing ρ_w without NIR adj. (top) and with NIR adjustment (bottom) versus in situ data (MERMAID clear waterdataset - bands 510, 560, 665)

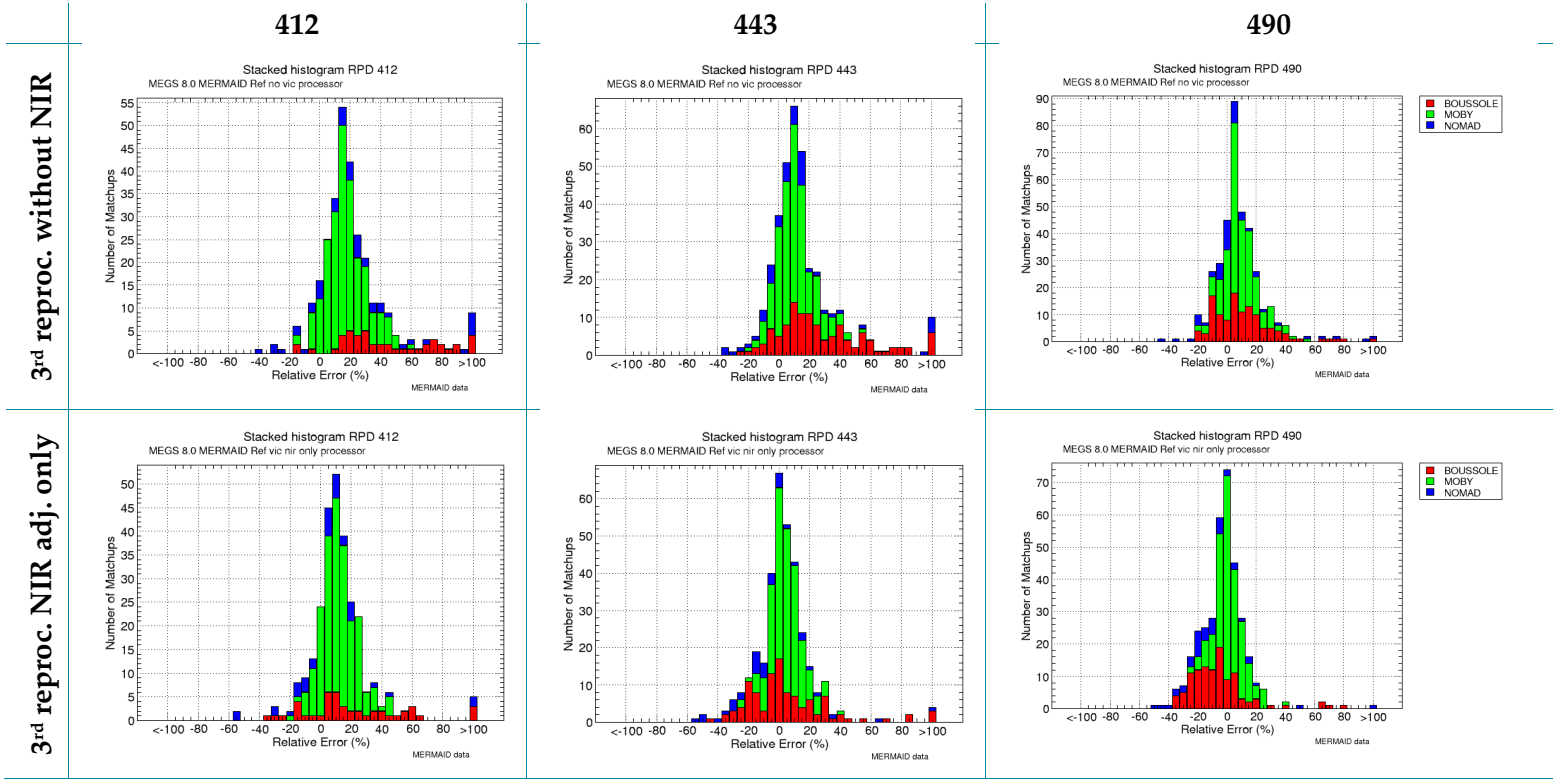

Figure 14: Histograms of 3rd reprocessing ρ_w relative errors without NIR adj. (top) and with NIR adjustment (bottom)

(MERMAID clear waterdataset - bands 412, 443, 490)

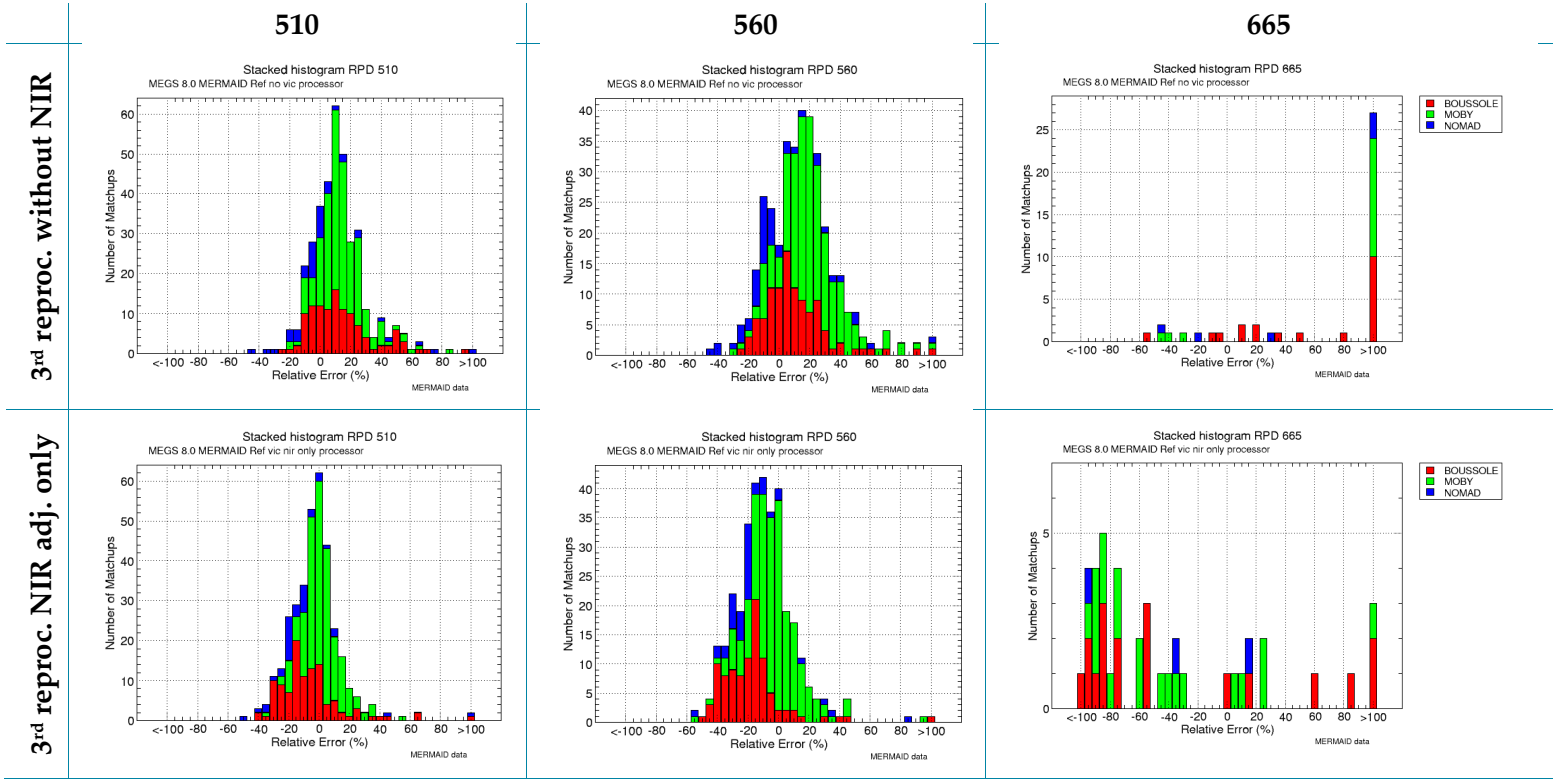

Figure 15: Histograms of 3rd reprocessing ρ_w relative errors without NIR adj. (top) and with NIR adjustment (bottom)

(MERMAID clear waterdataset - bands 510, 560, 665)

4.1.2 Adjustment in the VIS

4.1.2.1 Choice of the datasets

For reasons already mentioned in section 2.4, the *in situ* datasets for vicarious adjustment have been selected with respect to their representativeness of world ocean Case 1 waters. We have chosen the MOBY (Clark *et al.* 2003) and BOUSSOLE (Antoine *et al.* 2006, Antoine *et al.* 2008) buoys for they provide the longest time series of quality checked data in such conditions. Matchups extractions were made from the MERMAID system available at http://hermes.acri.fr/mermaid. A reason to consider two sites is to dispose of the maximum of reference optical measurements. As we shall see hereafter, this approach is *a posteriori* validated thanks to a good consistency in the gain factors from the two sites.

4.1.2.2 The BOUSSOLE dataset

The BOUSSOLE mooring (BOUée pour l'acquiSition de Séries Optiques à Long termE) is in operation since 2003 and located in the Ligurian Sea (Western Mediteranean – 7°54”East, 43°22”N) at depth of 2440m. Oligotrophic conditions prevail during summer with Chl-a ranging from 0.05-0.1 mg.m-3. The higher concentration can be observed during early spring bloom (February to April) with peaks of up to 5 mg.m-3. Concentrations between 0.1 and 0.2mg.m-3 characterize the other periods of the year (Antoine *et.al.* 2008). BOUSSOLE site presents permanently Case 1 waters characteristics.

BOUSSOLE measures upward and downward plane irradiance and nadir upwelling radiance (respectively E_u, E_d and L_u) at two depth as well as above surface solar irradiance (E_s). A full description of the theoretical work, practical design and construction, laboratory and *in situ* testing of the buoy, along with a description of the instrument suite and of some aspects of the data processing are presented by Antoine *et al.* 2008. The main steps are as follows. $L_u(\lambda,0^-)$ is extrapolated for the shallowest measurements as a function of K_L (diffuse attenuation coefficient for the upwelling nadir radiance), θ_s and chlorophyll concentration. KL is calculated for the two depth Lu measurements. $L_u(\lambda,0^-)$ is then corrected for instrument self-shading. From $L_u(\lambda,0^-)$, the $L_w(\lambda)$ is calculated through signal propagation across the air/sea interface. ρw(λ) can then be calculated after Es(λ) tilt correction.

4.1.2.3 The MOBY dataset

The Marine Optical BuoY (MOBY - Clark *et al.*, 2003) has been moored since 1996 in the vicinity of Hawaii and measures up welling radiance $L_u(\lambda)$ and down welling irradiance, $E_d(\lambda)$ over the spectral range 340nm to 955nm with 0.5nm spectral resolution at 1, 5 and 9m depth. MOBY also measure the surface irradiance $E_s(\lambda)$ through a collector on top of the buoy. Full details on the MOBY system can be found in Clark *et al.* 2003. Data processing include extrapolation of $L_u(\lambda,z)$ to $L_u(\lambda,0^-)$ through the computation of up-welling radiance attenuation coefficient. $L_u(\lambda,0^-)$ can then be propagated across the air/sea interface to

compute $L_w(\lambda)$. Although MOBY is primarily designed for the NASA sensors SeaWiFs and MODIS, the hyperspectral data are also processed for MERIS bands. MERMAID database make use of $L_w(\lambda)$ and $E_s(\lambda)$ measured at MOBY to compute $\rho_w(\lambda)$. No tilt correction is accounted for in MOBY data processing.

4.1.2.4 Data screening

The matchup selection procedure for visible band gain computation follows a similar procedure as for NIR band. The MERIS data matching *in situ* measurements are extracted on a 5x5 macro pixel if the surrounding 15x15 macro-pixel do not present any Cloud, Ice Haze, Medium or High Glint flag. The time difference should not exceed three hours between *in situ* measurement and satellite overpass. From 847 and 1104 matchups initially available in MERMAID above BOUSSOLE and MOBY respectively, this procedure ends up in with the selection of 60 and 70 reference points.

4.1.2.5 Gain factors computation

The procedure for computing VIS gain factors has already been described in equation 5 (building the reference TOA signal) and equation 3 (individual gain computation). It is noteworthy to recall that the NIR adjustment is applied for processing the VIS matchups dataset. Time series of gains at all wavelengths are displayed on Figure 16 and averaged values are provided in Table 4.

Table 4: Averaged gains, standard deviation and number of matchups used for computation

Band (nm)	Gain	Std-dev	N
412	0.9868	0.0093	78
443	0.9924	0.0092	105
490	0.9991	0.0105	108
510	1.0003	0.0107	113
560	1.0045	0.0097	112
620	1.0082	0.0060	67
665	1.0074	0.0069	106
681	1.0063	0.0059	94
709	1.		
753	1.0033	0.0030	1339
761	1.		
779	1.		
865	0.9864	0.0064	1339
885	0.9829	0.0102	1339
900	1.		

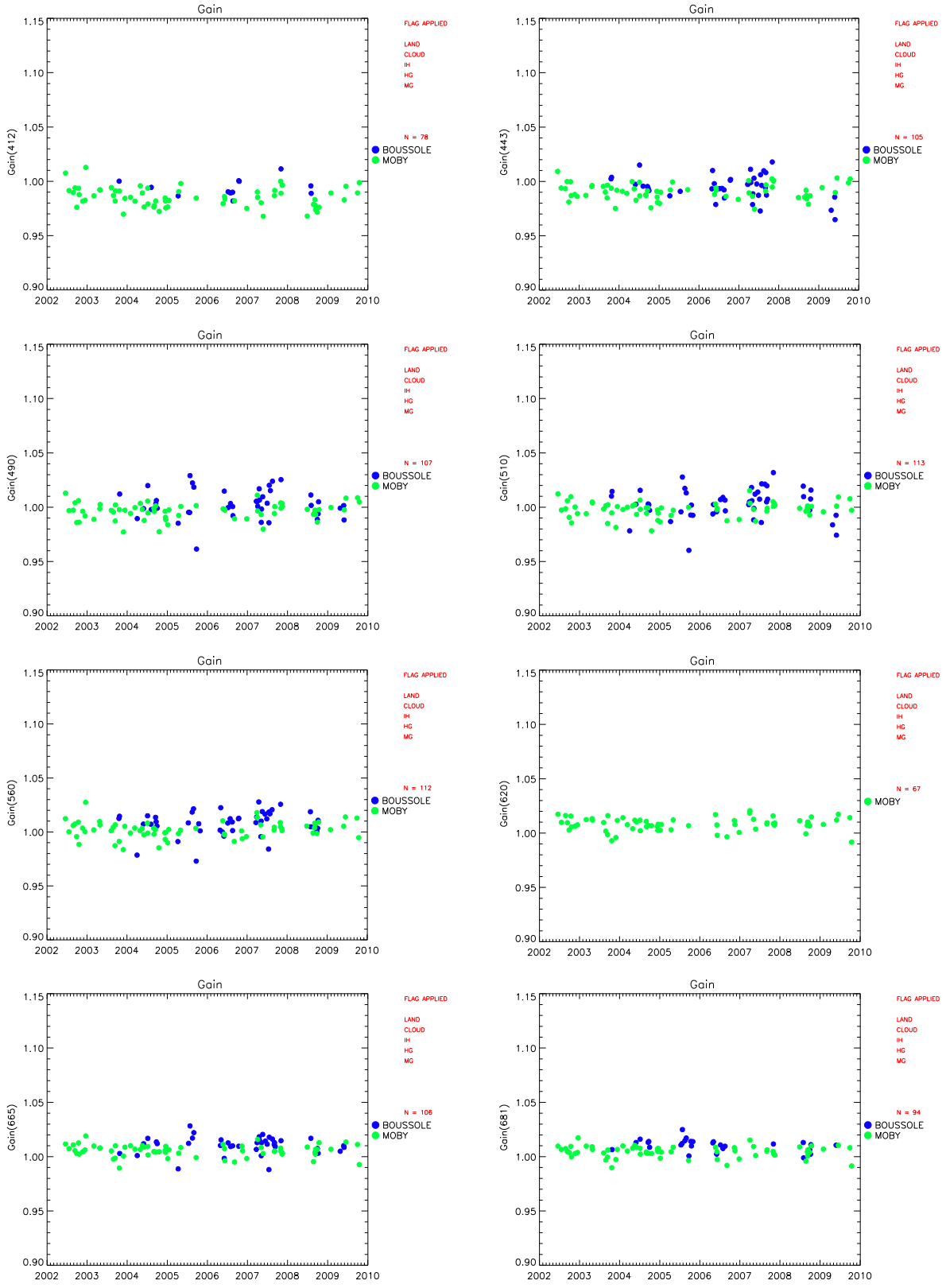

Figure 16: Gain time series

Inspection of the individual gains plotted in Figure 16 shows no temporal trends along the whole mission. The dispersion is noticeable but extremely close to that of SeaWiFS for instance (standard deviations in Table 4 to be compared to *e.g.* to 0.009 at 412 nm and 443 nm and 0.007 at 670 nm in Franz *et al.* 2007).

Some adjustment factors at BOUSSOLE are noisier, at 490 nm notably, but the average level is consistent with MOBY. It could come from a more complex atmosphere, closer to urban environment.

The spectral shape of the averaged gains, depicted on Figure 17, highlights the fact the adjustment is always lower than 2% and illustrates a good agreement with the Level 1 diffuser calibration. It is clear that the gains in the red are questionable, by assumption made at 709 and 779 nm.

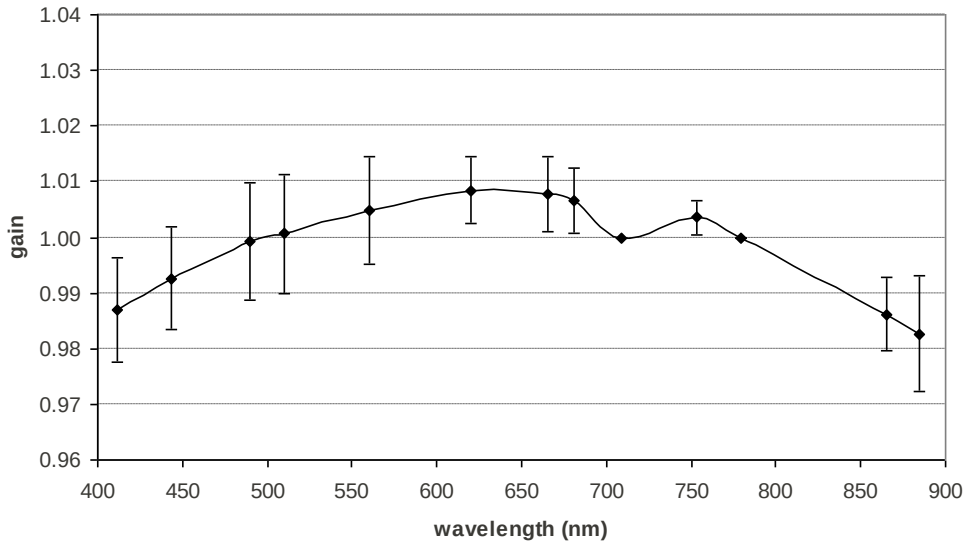

Figure 17: Gain spectra and related standard deviation implemented in MERIS 3rd reprocessing

4.1.2.6 Impact of in situ uncertainties on the gains

Although the variability in the MERIS gain factors is analogous to the one of *e.g.* SeaWiFS, we have tried to understand how the *in situ* uncertainties contribute to the global error budget and in particular how MOBY and BOUSSOLE datasets differ. For this we consider that the total standard deviation σ_g of the gains distribution results independently from the *in situ* and atmospheric correction uncertainties:

$$\sigma_g^2 = \left(\sigma_g^{IS}\right)^2 + \left(\sigma_g^{AC}\right)^2$$

Here σ_g^{IS} represents the standard deviation in the gains due to an uncertainty σ^{IS} on $\rho_w^{in\ situ}$. It can be computed by varying randomly this signal in equation 5 with associated standard deviation σ^{IS}. On the contrary, σ_g^{AC} represents the dispersion of the gains only due to uncertainties in atmospheric correction (*i.e.* resulting from ρ_{path}^{vic} and t_d^{vic}, see equation 5),

as if the reference signal $\rho_w^{in\ situ}$ were idealy measured; this term can be computed a posteriori by knowledge of σ_g and σ_g^{IS}.

We have conducted such analysis on the MOBY and BOUSSOLE datasets separately, with known *in situ* uncertainties σ^{IS} at each band as input. The results summarised in Table 5 show that the gain dispersion at MOBY is well explained by the 5% uncertainties in optical measurements at least until 510 nm, with $\left(\sigma_g^{IS}\right)^2/{\sigma_g}^2 > 50\%$. This is not the case at BOUSSOLE, what suggests that most of the dispersion might come from atmospheric correction. It is noteworthy that maritime models are almost never selected over this buoy, and other models with steepest ANgström exponent may amplify NIR error propagation.

Table 5: Contribution of the in situ uncertainties to dispersion in vicarious gains, for MOBY (left table) and BOUSSOLE (right table) matchups.

Band	σ^{IS} (%)	σ_g^{IS}	$\left(\sigma_g^{IS}/\sigma_g\right)^2$ (%)
412	5.00	0.0066	64.41
443	5.00	0.0069	94.88
490	5.00	0.0073	104.41
510	5.00	0.0049	52.54
560	5.00	0.0030	22.08
620	5.00	0.0004	0.60
665	12.50	0.0005	1.07
681	?	?	?

Band	σ^{IS} (%)	σ_g^{IS}	$\left(\sigma_g^{IS}/\sigma_g\right)^2$ (%)
412	6.00	0.0032	15.87
443	6.00	0.0039	12.06
490	6.00	0.0058	24.90
510	6.00	0.0049	18.74
560	6.00	0.0041	17.06
620	∅	∅	∅
665	6.00	0.0007	1.29
681	6.00	0.0009	3.90

4.1.3 Validation

4.1.3.1 Impact on MERMAID matchups

This section presents a validation of the water reflectance after vicarious adjustment, against *in situ* data gathered into MERMAID. In order to assess the evolution of the MERIS data, we also provide comparable plots with the 2nd reprocessing (R2005).

In the following, it is important to notice that MOBY and BOUSSOLE's points used for computing the vicarious gains are totally removed in the validation.

Flags removed in the matchups are Cloud, Ice_haze, High_glint, PCD_1_13. Also we apply standard statistical screening in the macropixel (coefficient of variation lower than 0.15, removal of outliers at 1.5 standard deviation) as described in Werdell *et al.* 2007.

From Figure 18 to Figure 21, we first focus on clear water considering the MOBY, BOUSSOLE and NOMAD datasets; the latter comprising however coastal waters as well. The offset

observed in the 2nd reprocessing data is now clearly removed, and the relationship between *in situ* and remote-sensing data much improved (slope of linear regression above 0.9 at 412, 443, 490 nm and 0.8 at 560 nm). The number of points is globaly unchanged[1], except at 665 nm where it is lower. The vicarious adjustment in the visible is however not responsible, since results in the previous section show already degraded number of point with the 3rd reprocessing and no adjustment, and a gain greater than 1 in the VIS cannot be suspected for producing negative reflectance. Eventually, dispersion seems to be analogous as in the 2nd reprocessing.

Validation on the full MERMAID dataset is presented from Figure 22 to Figure 25. The global offset (intercept) is significantly diminished, while the slope is rather degraded. Also there is a decrease in the number of valid points, especially for the most coastal waters. We have checked that this is mainly produced by the NIR adjustment and its interaction with the BPAC. Hence, although the statistics on valid pixels are largely acceptable, we do not recommend to consider that the vicarious adjustment described above is the ultimate answer over coastal waters for the current processing chain.

[1] It is slightly bigger but the definition of PCD_1_13 has changed between 2nd and 3rd reprocessing, see the document http://earth.eo.esa.int/pcs/envisat/meris/documentation/meris_3rd_reproc/MERIS_3rd_Reprocessing_Changes.pdf

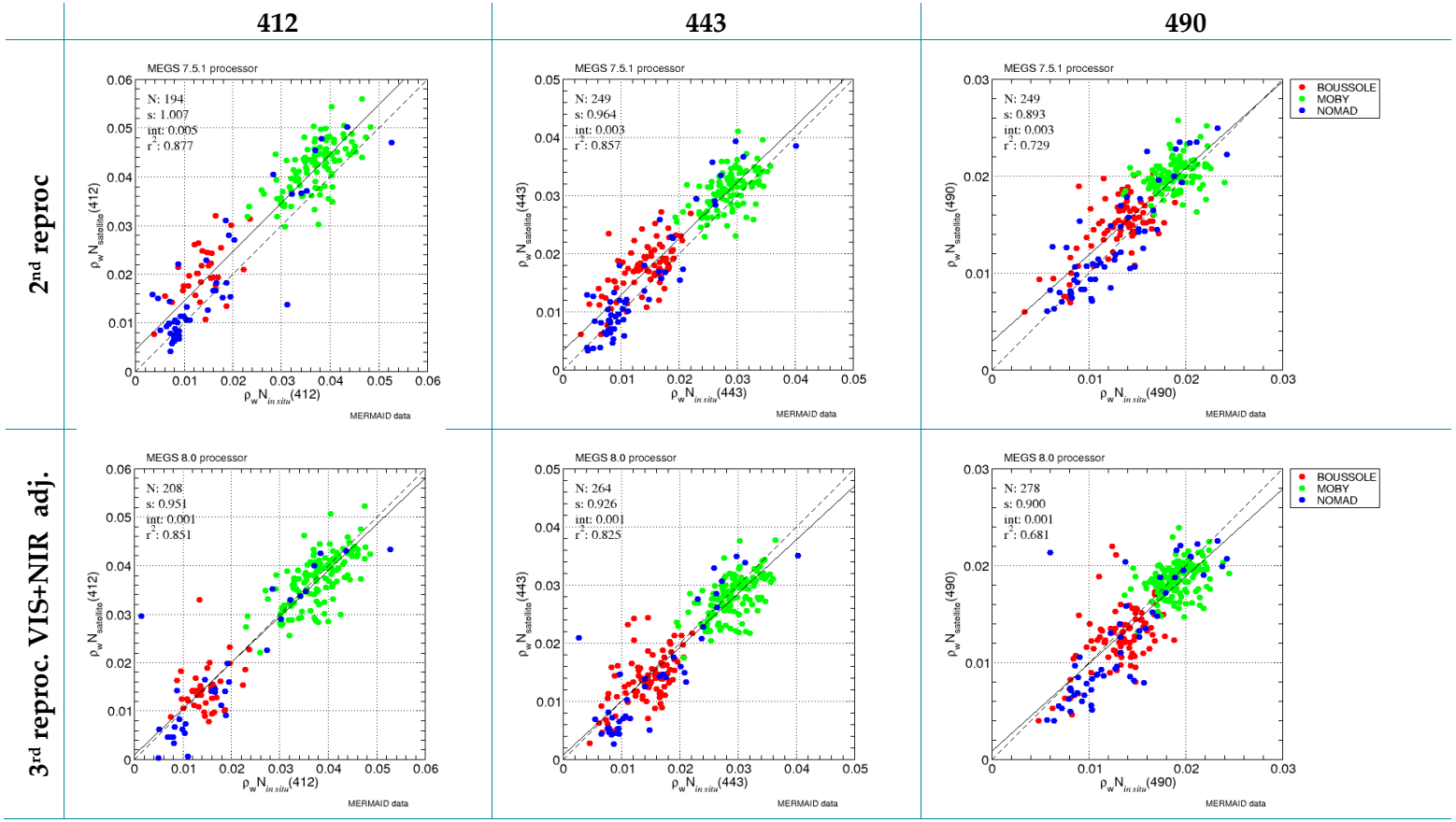

Figure 18: 2nd and 3rd reprocessing regression versus in situ data (MERMAID clear water dataset - bands 412, 443, 490)

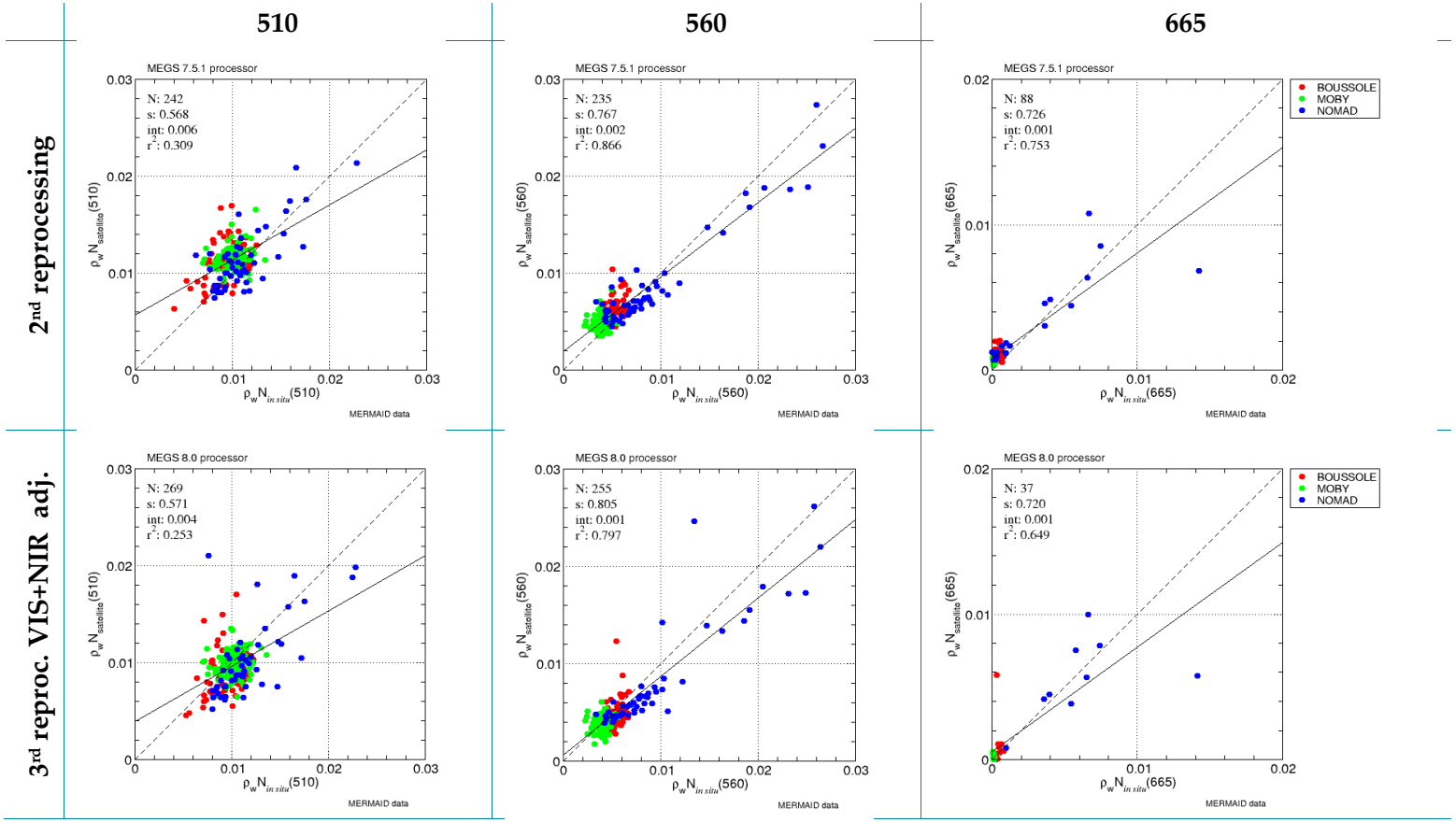

Figure 19: 2nd and 3rd reprocessing regression versus in situ data (MERMAID clear water dataset - bands 510, 560, 665)

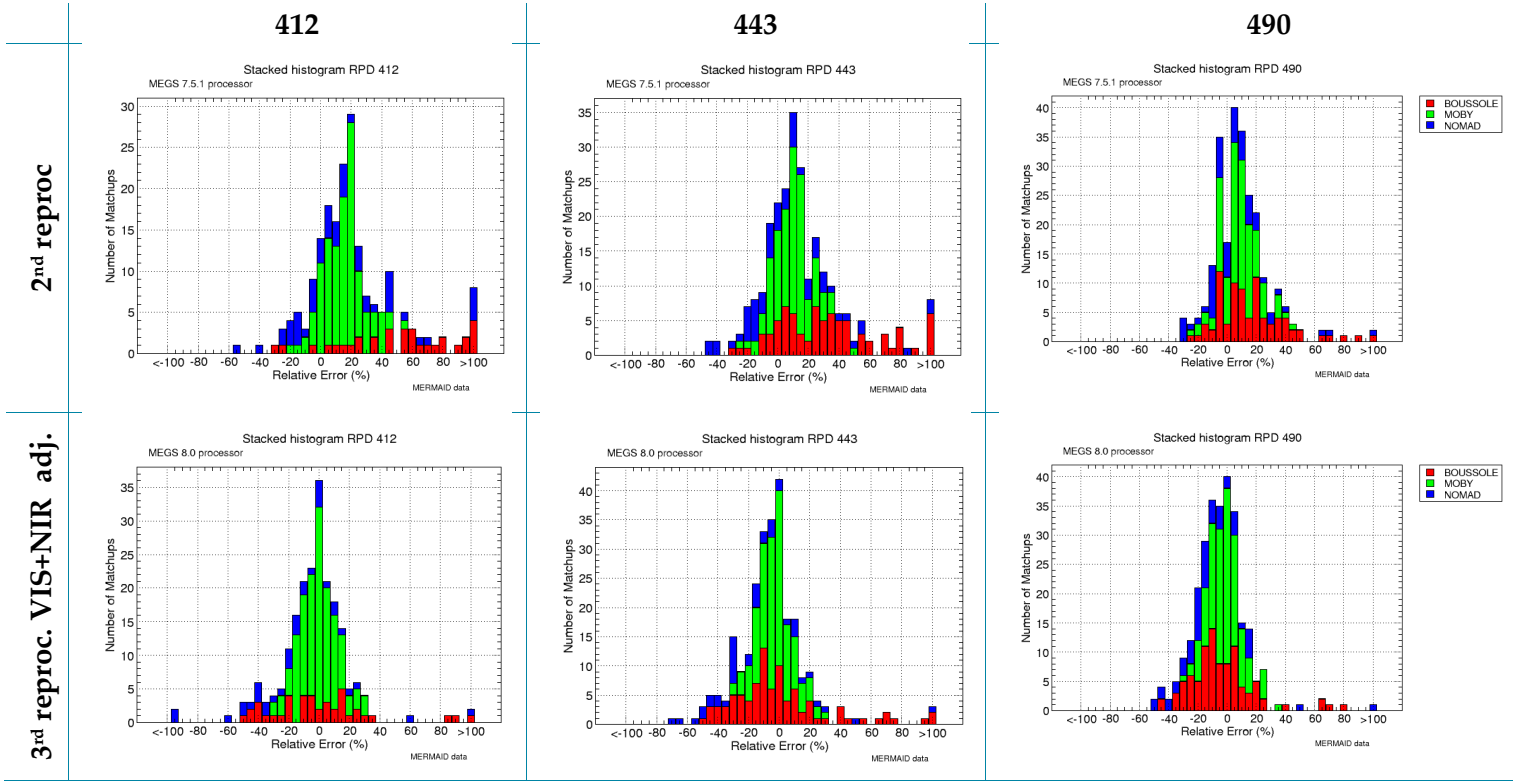

Figure 20: 2nd and 3rd reprocessing RPD stacked histograms (MERMAID clear water dataset - bands 412, 443, 490)

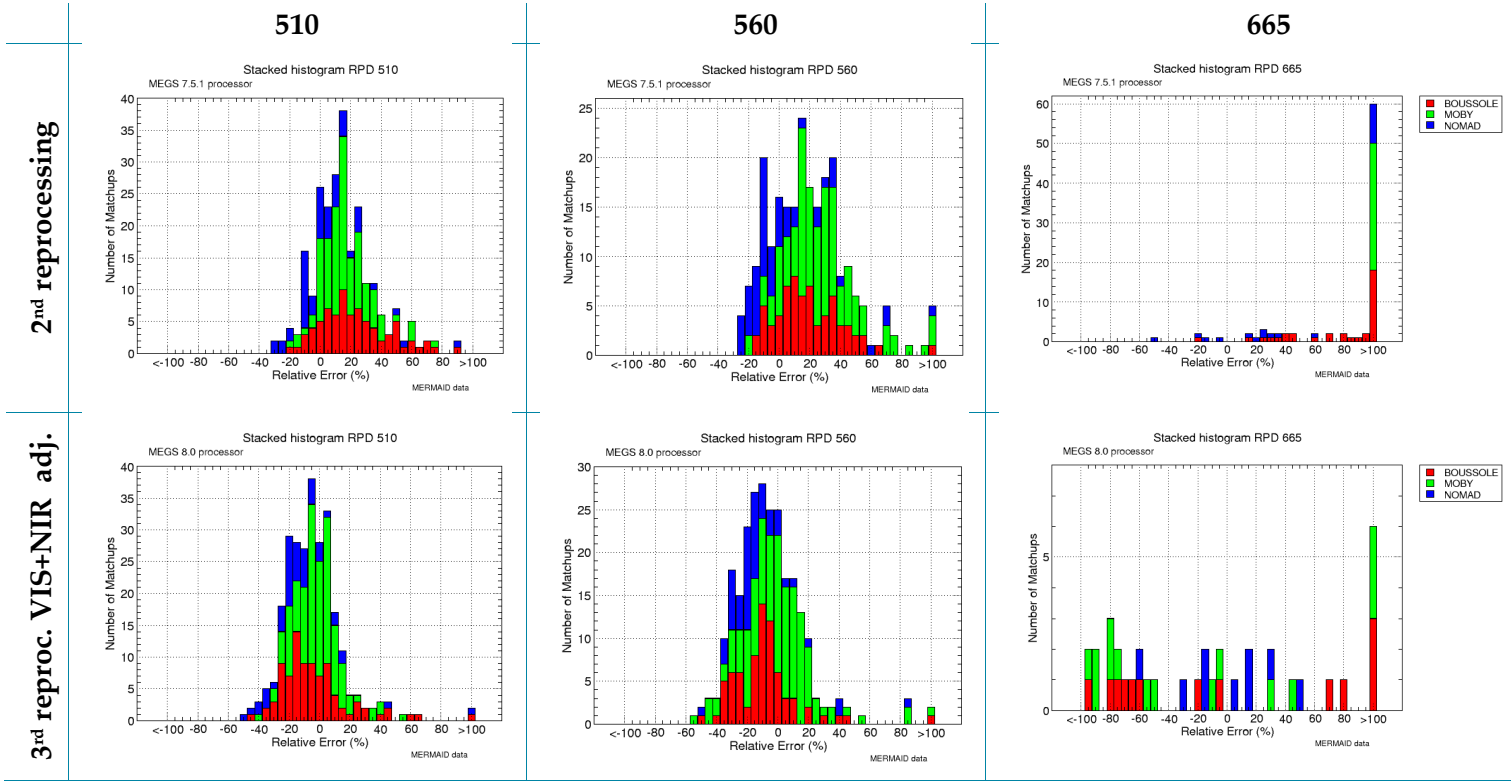

Figure 21: 2nd and 3rd reprocessing RPD stacked histograms (MERMAID clear water dataset - bands 510, 560, 665)

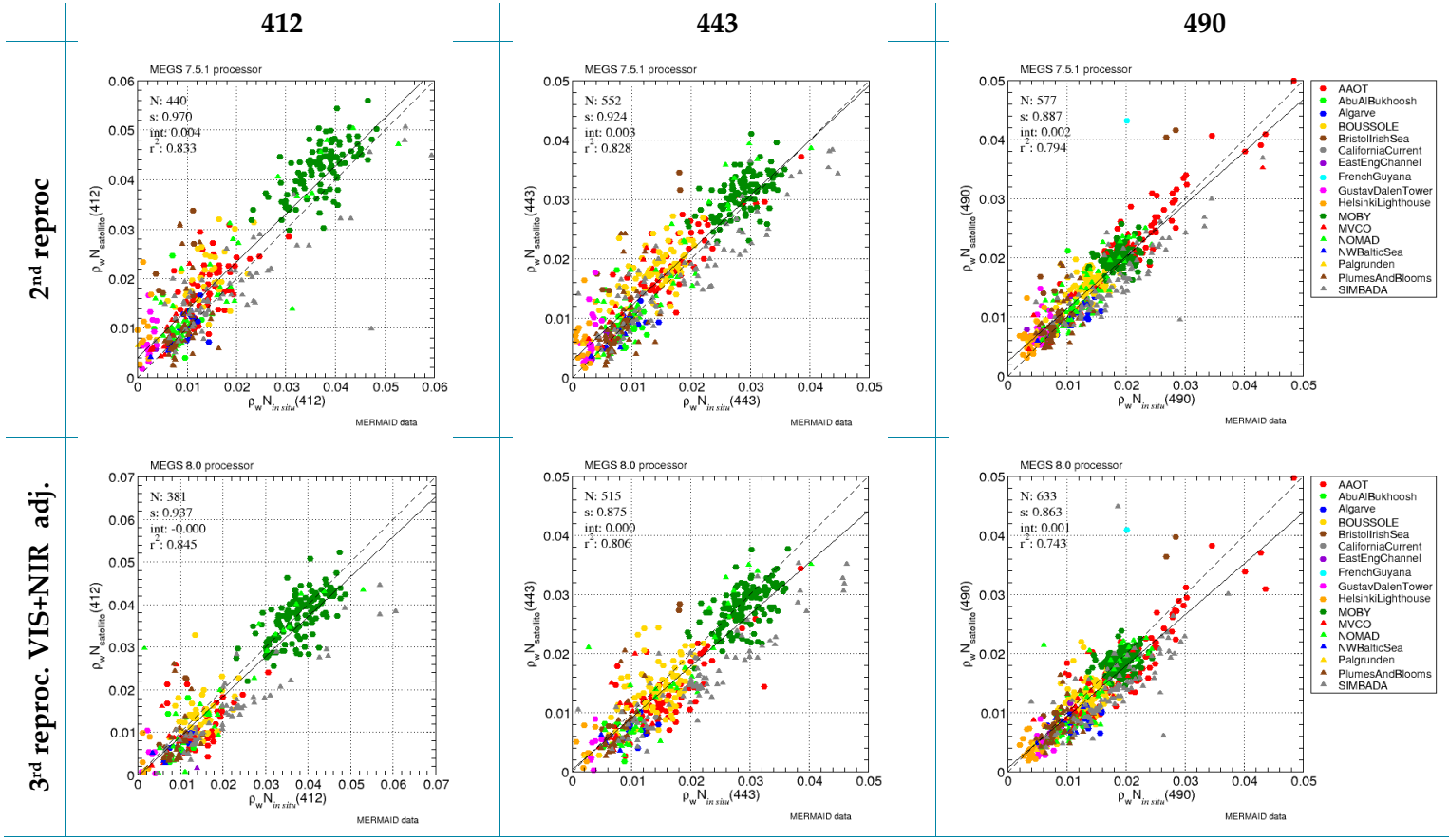

Figure 22: 2nd and 3rd reprocessing regression versus in situ data (MERMAID all dataset - bands 412, 443, 490)

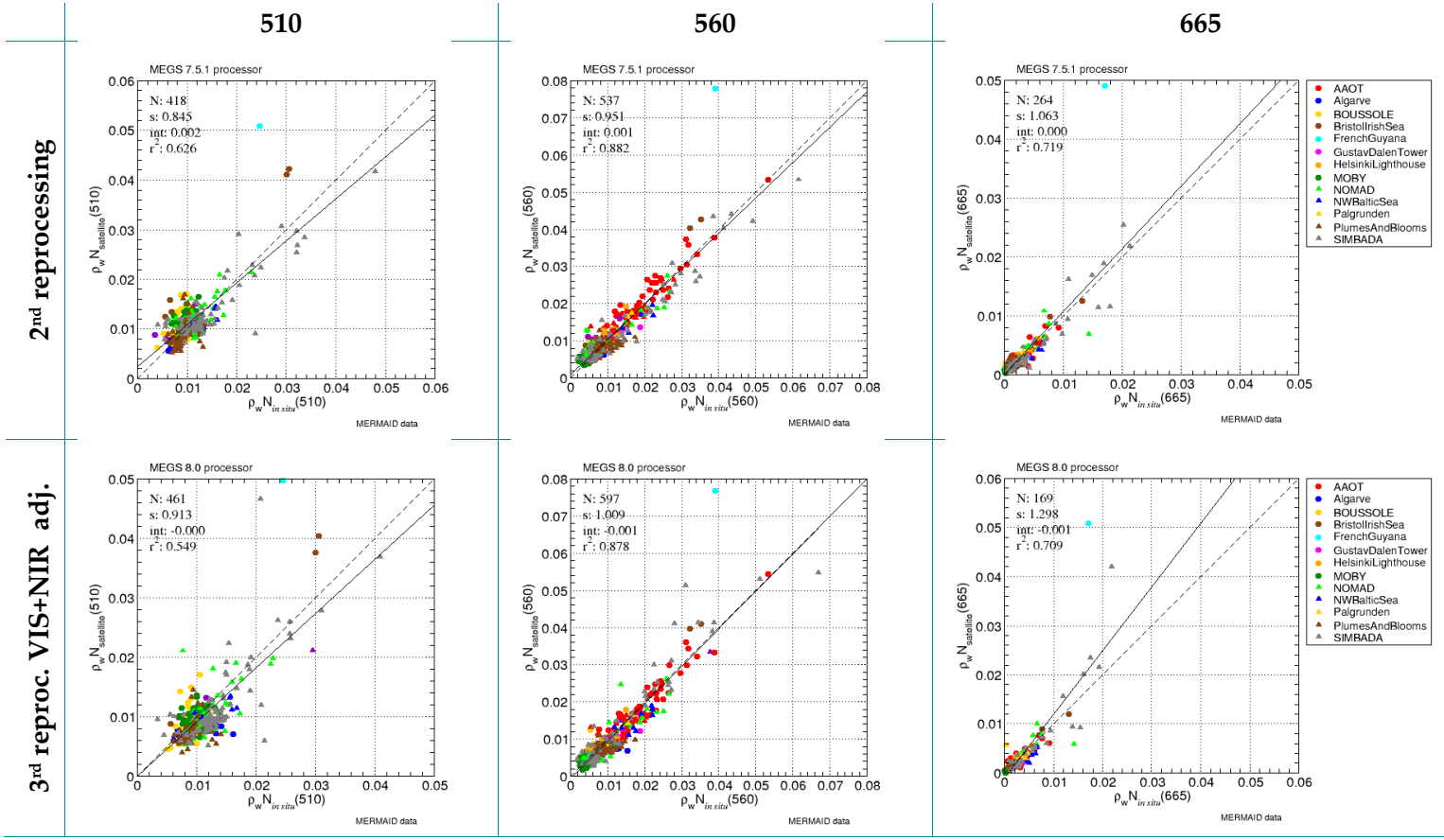

Figure 23: 2nd and 3rd reprocessing regression versus in situ data (MERMAID all dataset - bands 510, 560, 665)

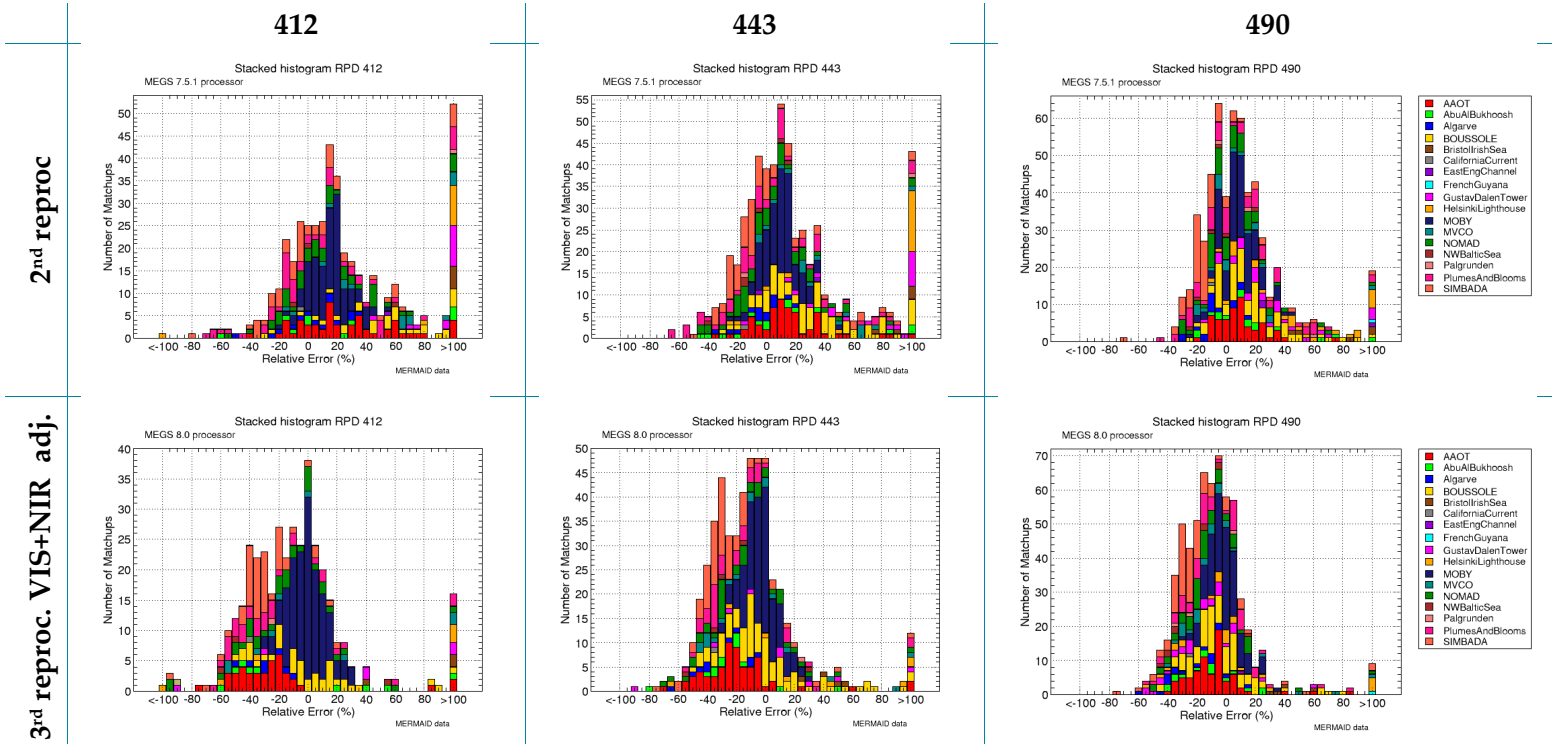

Figure 24: 2nd and 3rd reprocessing RPD stacked histograms (MERMAID all dataset - bands 412, 443, 490)

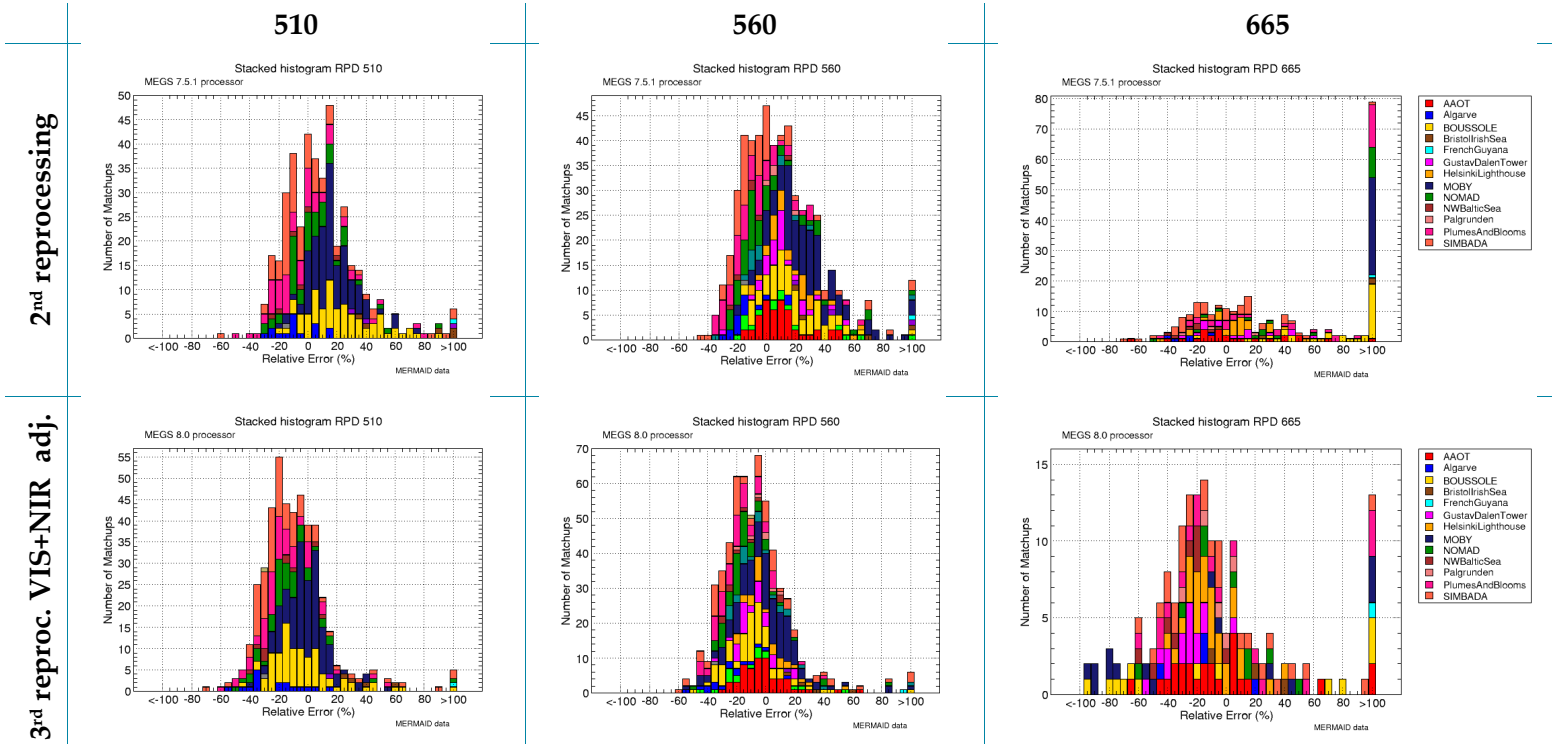

Figure 25: 2nd and 3rd reprocessing RPD stacked histograms (MERMAID all dataset - bands 510, 560, 665)

4.1.3.2 Comparison with NASA approach

We study here the comparison between our NIR gain approach (refered to SSA) with the published one in Franz *et. al* 2007 used for SeaWiFS and MODIS. We recall that this latter approach differs in two assumptions:

- a single band only is assumed to be perfectly calibrated (λ_{ref});
- the aerosol model over the calibration site is known and kept constant for the gain computation; it determines the spectral slope of the path signal.

It makes use of radiative transfer laws, for all aerosol models *ia*, first between the aerosol optical thickness τ_a and the total path reflectance ρ_{path}, and second of the spectral variation of the aerosol optical thickness. These relationships are already tabulated in the ground segment for the atmospheric correction and can be easily applied forwards or backwards. Formally, we can write the TOA modelling by the following equation, to be compared to equation 15 in the SSA approach:

$$\rho_{gc}(\lambda) = \rho_{path}(\lambda, \tau_a(\lambda), ia) + t\rho_w^{pw}(\lambda) \qquad (18)$$

From the knowledge of the aerosol model *ia* and $\rho_{gc}(\lambda_{ref})$, we can invert equation 18 to retrieve $\tau_a(\lambda_{ref})$, propagate it at any other wavelength λ and apply equation 18 to reconstruct $\rho_{gc}^t(\lambda)$ at any other band.

We have tested the five marine aerosol models[2] available in the MERIS ground segment and computed the NIR gains at SPG and SIO assuming a proper adjustment of $\lambda_{ref} = 779$ nm (Table 6). With the exception of model 0, all models end up with gain at 865nm lower that one. Aerosol models 3 and 4 produce the closest gains at 865nm and 885 nm in comparison to the SSA procedure (0.26% and 0.37% relative percent difference at 865 nm respectively). This is very consistent with the choice of Franz *et al.* relying on the maritime model with 90% relative humidity. Also the associated gains at 709 nm are very closed to the unity (1.0029 and 1.0001 respectively for models 3 and 4), which tends to support the assumption of the SSA that channels 709 nm and 779 nm are aligned.

[2] Aerosol assemblages 1 to 4 contain a fixed amount of continental aerosol in the tropospheric layer, with varying relative humidity of 50%, 70%, 90% and 99% respectively. Model 0 has no aerosol in the tropospheric layer and a relative humidity of 99%. See Zagolski 2011 for more details.

Table 6: Average gains computed with the fixed aerosol model procedure and SSA.

	Fixed Aerosol Model Procedure										SSP	
	model 0		model 1		model 2		model 3		model 4			
WL	**mean**	**stddev**	**mean**	**stddev**	**mean**	**stddev**	**mean**	**stddev**	**mean**	**stddev**	**mean**	**stddev**
709	0.9854	0.0062	1.0085	0.0089	1.0071	0.0082	1.0029	0.0068	1.0001	0.0066	1.0000	
753	0.9980	0.0040	1.0068	0.0050	1.0067	0.0050	1.0049	0.0042	1.0038	0.0039	1.0033	0.0030
779	1.0000		1.0000		1.0000		1.0000		1.0000		1.0000	
865	**1.0162**	**0.0099**	**0.9737**	**0.0134**	**0.9758**	**0.0124**	**0.9839**	**0.0109**	**0.9901**	**0.0117**	**0.9864**	**0.0064**
885	1.0204	0.0132	0.9666	0.0178	0.9693	0.0166	0.9802	0.0145	0.9875	0.0152	0.9829	0.0102

Figure 26 presents the time series of $g(865)$ with aerosol model 3, which has the weakest dispersion and is considered by NASA. Two remarkable features can be observed. First, the seasonal signal is very pronounced, and much more important than with the SSA (compare to Figure 6); second, the artefact on the OCL OFF period is not detected.

When the gains are plotted against geometry (see Figure 27), the seasonal effect appears by a higher standard deviations with sun zenith and scattering angles. This is the main reason to discard this procedure.

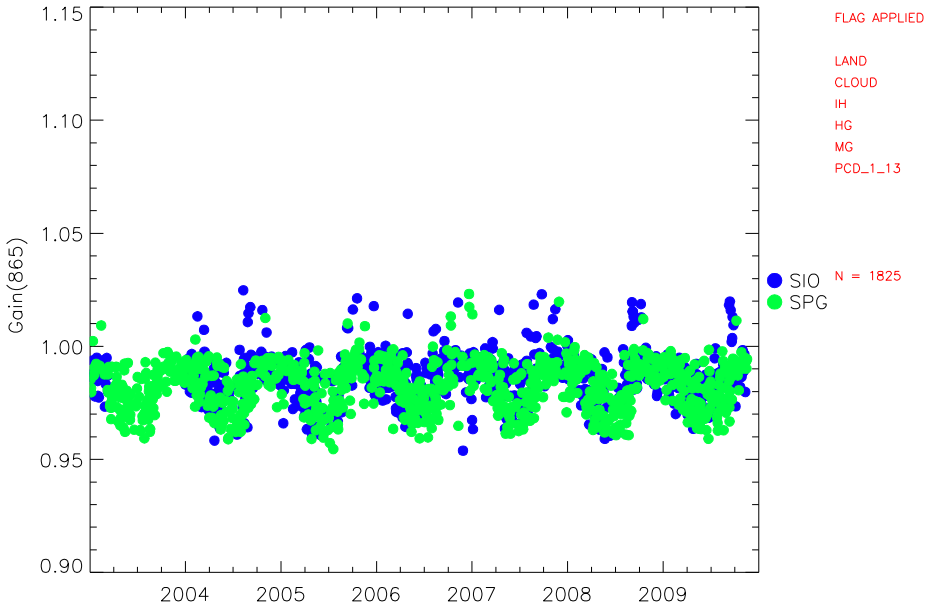

Figure 26: Time series of $g(865)$ at SIO (blue) and SPG (green) with the fixed aerosol approach (model 3).

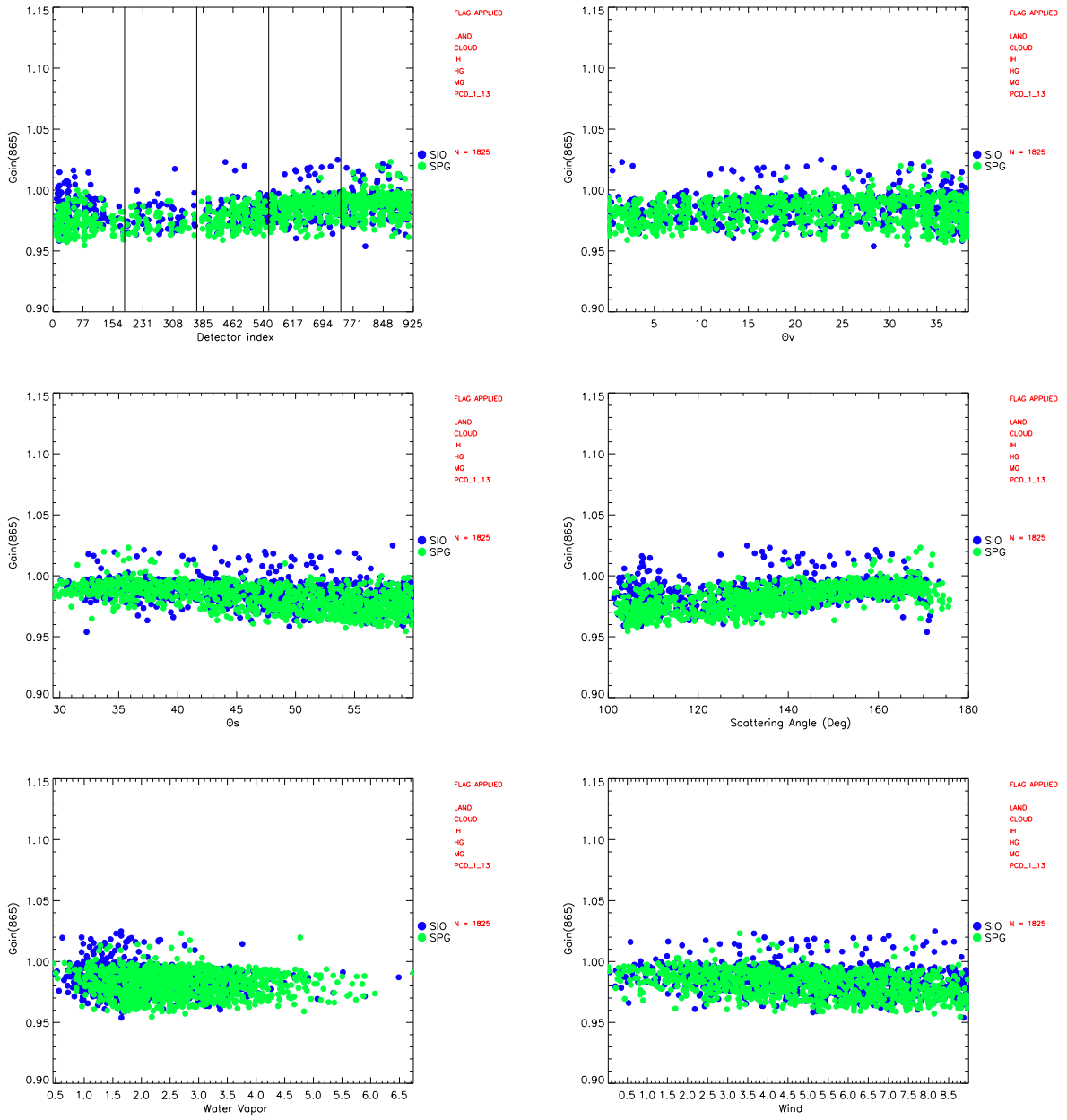

Figure 27: Variation of $g(865)$ at SIO (blue) and SPG (green) computed by the fixed aerosol approach (model 3), from top to bottom and left to right with detector index (vertical lines delimit camera 1 to 5), view zenith angle, sun zenith angle, scattering angle, water vapour and wind modulus

4.2 Practical consideration

The set of fifteen adjustment factors $\bar{g}(\lambda)$ are incorporated in a new field of the Ocean Aerosol ADF; see Volume 11 of the MERIS products specifications available at http://earth.eo.esa.int/pcs/envisat/meris/documentation/meris_3rd_reproc/.

Also, they can be read and changed in the ODESA processor for testing alternative values; see the ODESA quick start guide available at http://www.odesa-info.eu .

The vicarious adjustment globally decreases the level of water reflectance along the full spectrum; it is true also in the red despite VIS gains higher than one because of the NIR adjustment. Over very clear waters, it might lead to slightly negative reflectance (interpreted as noise around a virtually null reflectance) and raise the PCD_1_13 flag which rejects negative reflectance. In order to avoid this artefact, PCD_1_13 of the 3rd reprocessing includes now a threshold allowing small negative reflectance. More details are available on the document "MERIS 3rd reprocessing data reprocessing – Software and ADF update" available at http://earth.eo.esa.int/pcs/envisat/meris/documentation/meris_3rd_reproc/.

5 Assumption and limitation

- The vicarious adjustment in the VIS removes a systematic bias but cannot remove dispersion in the marine signal. Indeed by construction of the gains in the VIS, and whatever the NIR adjustment, we have

$$\rho_w^{vic}(\lambda) - \rho_w^{in\ situ}(\lambda) = \frac{\rho_{gc}(\lambda)}{t_d(\lambda)}\left(\bar{g}(\lambda) - g(\lambda)\right) \qquad (19)$$

  which shows that any dispersion in the gains yields to a dispersion in the water reflectance errors.

- The vicarious adjustment in the VIS cannot correct different biases of several datasets. This is clear by another formulation of the gain, from equation (4) and (5)

$$g(\lambda) = 1 - \left(\frac{t_d(\lambda)\,\rho_w^{in\ situ}(\lambda)}{\rho_{gc}(\lambda)}\right)\left(\frac{\rho_w(\lambda) - \rho_w^{in\ situ}(\lambda)}{\rho_w^{in\ situ}(\lambda)}\right) \qquad (20)$$

  where different relative errors on ρ_w from different datasets would produces inhomogeneous gains.

- The interaction between the vicarious adjustment in the NIR and the BPAC is complex. We have noticed that other implementations of the BPAC would be less sensitive and would not remove coastal matchups in the validation (not shown here).

- The present implementation computes a single factor at each band for the whole mission and all cameras. If much more reference data were available, a set of gains per camera could be studied.

- The vicarious adjustment is not just a sensor calibration, but an adjustment of the whole system sensor+processing chain (in particular atmospheric correction). It should be updated at every change in the Level1 or Level2 ground segment.

- The present approach is mainly justified for the open oceans where homogeneity in the targets and in the behavior of atmospheric correction helps to get a consistent unique set of spectral gains (equation 19 and 20). On the other hand, vicarious adjustment on coastal water would be by nature very local (see Zibordi and Mélin 2010) and not applicable operationally for the whole mission.

6 References

Antoine, D. and A. Morel, 1998. Relative importance of multiple scattering by air molecules and aerosols in forming the atmospheric path radiance in the visible and near-infrared parts of the spectrum, Applied Optics Vol. 37, No. 12, 2245 – 2259.

Antoine, D. and A. Morel, 1999. A multiple scattering algorithm for atmospheric correction of remotely-sensed ocean colour (MERIS instrument) : principle and implementation for atmospheres carrying various aerosols including absorbing ones, International Journal of Remote Sensing, 20, 1875-1916.

Antoine, D., M. Chami, H. Claustre, F. D'Ortenzio, A. Morel, G. Bécu, B. Gentili, F. Louis, J. Ras, E. Roussier, A. J. Scott, D. Tailliez, S. B. Hooker, P. Guevel, J.-F. Desté, C. Dempsey and D. Adams, 2006. BOUSSOLE: a joint CNRS-INSU, ESA, CNES and NASA Ocean Color Calibration And Validation Activity. NASA Technical memorandum N° 2006 – 214147.

Antoine, D., P. Guevel, J.-F. Desté, G. Bécu, F. Louis, A.J. Scott and P. Bardey, 2008. The «BOUSSOLE» buoy, a new transparent-to-swell taut mooring dedicated to marine optics: design, tests and performance at sea, Journal of Atmospheric and Oceanic Technology, 25, 968-989.

Antoine, D., F. D'Ortenzio, S. B. Hooker, G Bécu, B. Gentili, D. Tailliez, and A. J. Scott, 2008. Assessment of uncertainty in the ocean reflectance determined by three satellite ocean color sensors (MERIS, SeaWiFS and MODIS-A) at an offshore site in the Mediterranean Sea (BOUSSOLE project), Journal of Geophysical Research, 113, C07013, doi:10.1029/2007JC004472.

Antoine, D. and A. Morel, 2011. Atmospheric Correction of the MERIS observations over Ocean Case 1 waters, MERIS ATBD 2.7, Issue 5, revision 1, July 2011.

Barker K., Huot J.P., Goryl, P., 2010. MERIS Optical Measurement Protocols, Part A: In Situ reflectance measurements. ESA - CO-SCI-ARG-TN-008, pp93.

Bailey, S. W., B. H. Hooker, D. Antoine, B. A. Franz and P. J. Werdell, 2008. Sources and assumption for the vicarious calibration of ocean color satellite observations, Applied Optics Vol. 47, No. 12, 2035 – 2045.

Clark, D. K., H. R. Gordon, K. J. Voss, Y. Ge, Y., W. Broenkow and C. Trees, 1997. Validation of Atmospheric Correction Over the Oceans. Journal of Geophysical Research 102D: 17209-17217.

Clark, D. K., M. A. Yarborough, M. E. Feinholz, S. Flora, W. Broenkow, Y. S. Kim, B. C. Johnson, S. W. Brown, M. Yuen, and J. L. Mueller, 2003. MOBY, A Radiometric Buoy for Performance Monitoring and Vicarious Calibration of Satellite Ocean Colour Sensors: Measurements and Data Analysis Protocols. In Ocean Optics Protocols for Satellite Ocean Colour Sensor Validation, NASA Technical Memo. 2003-211621/Rev4, VolVI, 3-34 (Eds J. L. Muller, G. Fargion and C. McClain). Greenbelt, MD.: NASA/GSFC.

Cox, C. and W. Munk, 1954. Statistics of the sea surface derived from Sun glitter, Journal of Marine Research, 13, 198 – 227.

Cox, C. and W. Munk, 1954. Measurement of the Roughness of the Sea Surface from Photographs of the Suns Glitter. J. Opt. Soc. Am. 44, 838 – 850.

Cristina, S., P. Goela, J. I. Icely, A. Newton and B. Fragoso, 2009. Assessment of water-leaving reflectance of the oceanic and coastal waters using MERIS satellite products off the southwest coast of Portugal. Journal of Coastal Research Special Issue (56): 5.

Ebuchi, N. and S. Kizu, 2002. Probability Distribution of Surface Wave Slope Derived Using Sun Glitter Images from Geostationary Meteorological Satellite and Surface Vector Winds from Scatterometers. J. Oceanogr. 58, 477 – 486.

Eplee, R. E. Jr., W. D. Robinson, S. W. Bailey, D. K. Clark, P. J. Werdell, M. Wang, R. A. Barnes, and C.R. McClain, 2001. Calibration of SeaWiFS. II. Vicarious techniques, Appl. Opt. 40, 6701 – 6718.

Franz, B. A., E. J. Ainsworth and S. W. Bailey, 2001. SeaWiFS, vicarious calibration: an alternative approach utilizing simultaneous *in situ* observations of oceanic and atmospheric optical, properties, NASA Tech. Memo. 209982, National Aeronautics, and Space Administration, Goddard Space Flight Center, Greenbelt, MD.

Franz, B. A., S. W. Bailey, J. Werdell, Ch. McClain, 2007. Sensor-independent approach to the vicarious calibration. of satellite ocean color radiometryc. Applied Optics, Vol. 46, No. 22, 5068 – 5082.

Gordon, H. R and M. Wang, 1994. Retrieval of water-leaving radiance and aerosol optical thickness over the oceans with SeaWiFS: a preliminary algorithm, Appl. Opt. 33, 443 – 452.

Gordon, H. R., 1997. Atmospheric correction of ocean color imagery in the Earth observing system era, J. Geophys. Res. 102D, 17081 – 17106.

Gordon, H. R., 1998. In-orbit calibration strategy for ocean color sensors, Remote Sens. Environ. 63, 265 – 278.

Holben, B. N., T. F. Eck, I. Slutker, D. Tanré, J. P. Buis, A. Setzer, E. Vermote, J. A. Reagan, Y. J. Kaufman, T. Nakajima, F. Lavenu, I. Jankowiak and A. Smirnov, 1998. AERONET – A federated instrument network and data archive for aerosol characterisation, Remote Sens. Environ. 66, 1 – 16.

Hooker, S. B. and C. R. McClain, 2000. The calibration and valida-tion of SeaWiFS data, Prog. Oceanogr. 45, 427 – 465.

Hooker, S. B., W. E. Esaias, G. C. Feldman, W. W. Gregg and C. R. McClain, 1992. An overview of SeaWiFS and ocean color, NASA Tech. Memo. 104566, National Aeronautics and Space Administration, Goddard Space Flight Center, Greenbelt, MD.

Kneubühler, M., M. Schaepman, K. Thome, F. Baret, A. Müller, 2002. Calibration and validation of ENVISAT MERIS part 1: vicarious calibration at Rail Road Valley Playa (NV). Proceeding of the Envisat Validation Workshop 9-13 December 2002, ESRIN, Frascati, Italy.

Kratzer, S., C. Brockmann and G. F. Moore, 2008. Using MERIS full resolution data (300 m spatial resolution) to monitor coastal waters– a case study from Himmerfjärden, a fjord-like bay in the north-western Baltic Sea. Remote Sensing of the Environment 112(5): 2284-2300.

Loisel, H., X. Mériaux, A. Poteau, L. F. Artigas, B. Lubac, A. Gardel, J. Caillaud, and S. Lesourd, 2007. Analyze of the inherent optical properties of French Guiana coastal waters for remote sensing applications. Journal of Coastal Research SI 56 (Proceedings of the 10th International Coastal Symposium), 1532 – 1536.

Lubac B. and H. Loisel, 2007. Variability and classification of remote sensing reflectance spectra in the Eastern English Channel and southern North Sea. Remote Sensing of Environment 110, 45-58.

Mélin F. and G. Zibordi, 2010. Vicarious calibration of satellite ocean color sensors at two coastal sites, Applied Optics, vol 49 n°5, pp798 – 810.

Moore, G. and S. Lavender, 2011. Case IIS Bright Pixel Atmospheric Correction, MERIS ATBD 2.6, Issue 5.0, June 2011.

Rast, M. and J.-L. Bezy, 1999. The ESA Medium Resolution Imaging Spectrometer MERIS: A review of the instrument and its mission. International Journal of Remote Sensing, 20(9), 1681 − 1702.

Ruddick, K. G., V. De Cauwer, Y. Park and G. Moore, 2006. Seaborne measurements of near infrared water-leaving reflectance - the similarity spectrum for turbid waters. Limnology and Oceanography 51(2): 1167-1179.

Santer, R. and F. Zagolski, 2010. The MEROS database and the forward mode, ESA Internal Technical Note, May 2010

Werdell, P. J. and S. W. Bailey, 2005. An improved bio-optical data set for ocean color algorithm development and satellite data product validation. Remote Sensing of Environment, 98(1), 122-140.

Zagolski, F., 2011. Specification of the Scientific Contents of the MERIS Level1-b and Level 2 Auxiliary Data Products, Document n° PO-RS-PAR-GS-002, Issue 3, 27-Feb-2011, http://envisat.esa.int/instruments/meris/rfm/PO-RS-PAR-GS-0002-3C-Prod_Spec.pdf.

Zibordi, G., F. Mélin, and J.-F. Berthon, 2006. Comparison of SeaWiFS, MODIS and MERIS radiometric product at a coastal site, Geophysical research letters, vol 33, L06617, doi: 10.1029/2006GL025778

G. Zibordi, B. Holben, I. Slutsker, D. Giles, D. D'Alimonte, F. Mélin, J.-F. Berthon, D. Vandemark, H. Feng, G. Schuster, B. Fabbri, S. Kaitala, J. Seppälä, 2009. AERONET-OC: a network for the validation of Ocean Color primary radiometric products. Journal of Atmospheric and Oceanic Technology, 26, 1634-1651.

G. Zibordi, J.-F.Berthon, F.Mélin, D. D'Alimonte and S.Kaitala, 2009. Validation of satellite ocean color primary products at optically complex coastal sites: northern Adriatic Sea, northern Baltic Proper and Gulf of Finland. Remote Sensing of Environment, 113, 2574-2591.

End of Document